Astronomy & Astrophysics manuscript no. aanda
October 14, 2025

Resolving stellar populations, star formation, and ISM conditions with JWST in a large spiral galaxy at $z \approx 2$

Eleonora Parlanti[1,2⋆], Giulia Tozzi[1⋆], Natascha M. Förster Schreiber[1], Claudia Pulsoni[1], Letizia Scaloni[1,3,4], Stavros Pastras[1,5], Pascal Oesch[6,7], Capucine Barfety[1], Francesco Belfiore[8], Jianhang Chen[1], Giovanni Cresci[9], Ric Davies[1], Frank Eisenhauer[1,10], Juan M. Espejo Salcedo[1], Reinhard Genzel[1,11], Rodrigo Herrera-Camus[12], Jean-Baptiste Jolly[1], Lilian L. Lee[1], Minju M. Lee[7,13], Daizhong Liu[14], Dieter Lutz[1], Filippo Mannucci[9], Giovanni Mazzolari[1], Thorsten Naab[5], Amit Nestor Shachar[15], Sedona H. Price[16], Alvio Renzini[17], Taro T. Shimizu[1], Amiel Sternberg[15], Martina Scialpi[1,18,19,9], Eckhard Sturm[1], Linda J. Tacconi[1], Hannah Übler[1], Stijn Wuyts[20]

(Affiliations can be found after the references)

ABSTRACT

Cosmic noon represents the prime epoch where today's massive galaxies assembled most of their stellar mass, and a sweet spot for observations with both the space-based *James Webb Telescope* (JWST) and ground-based near-IR integral-field unit (IFU) spectrographs. This work analyses JWST NIRSpec Micro Shutter Array (MSA), NIRCam Wide Field Slitless Spectroscopy (WFSS) of K20-ID7, a large spiral, star-forming (SF) galaxy at $z = 2.224$, with evidence for radial gas inflows. By exploiting the synergy with ground-based IFU ERIS observations, we conduct a comprehensive and resolved study of the interstellar medium (ISM) and stellar properties of this galaxy, from rest-frame optical to near-IR, through several emission-line diagnostics, resolved spectral energy distribution (SED) fitting of high-resolution imaging, and Paβ line detection in NIRCam WFSS data. Our analysis reveals massive ($M_\star \simeq (0.67-3.5)\times10^9$ M$_\odot$) SF clumps with star formation rates (SFRs) spanning about the range 3−24 M$_\odot$ yr^{-1}, and quite low values of dust attenuation ($A_V \simeq 0.4$), electron density ($n_e \lesssim 300$ cm^{-3}), and ionisation parameter ($\log(U) \simeq -3.0$). The central bulge turns out to be modest-massive ($M_\star = (7\pm3)\times10^9$ M$_\odot$), heavily obscured ($A_V = 6.43\pm0.55$), and likely to have formed most of its stellar mass in the past (SFR = 82 ± 42 M$_\odot$ yr^{-1} over the last ∼ 100 Myr), yet still forming stars at a lower rate (SFR = 12 ± 8 M$_\odot$ yr^{-1} over the last ∼ 10 Myr). In terms of chemical abundances, we infer a relatively low sulfur abundance log(S/O)≃ -1.9, with possible implications on the production of sulfur via Type I supernova explosions. Moreover, all distinct galaxy regions feature a metallicity $12+\log(O/H) \approx 8.54$, which is a likely consequence, along with the apparent enhancement of the N/O abundance (i.e. log(N/O)≃ −1.0), of dilution effects due to radial inflows of metal-poor gas. Finally, the radial profile in stellar age and the Hα equivalent width measured in distinct galaxy regions show signs of older stellar population in the inner galaxy regions compared to the outskirts, pointing to an inside-out growth of K20-ID7.

Key words.

1. Introduction

Present-day massive galaxies assembled half of their current mass at $z \sim 1-3$ – the so-called "cosmic noon" epoch –, during which the star formation rate (SFR) density of the Universe reached its peak ($z \approx 2$; Madau & Dickinson 2014), thanks to the large amount of available gas (Tacconi et al. 2020; Walter et al. 2020). At this epoch, gas-rich, turbulent star-forming disks represent the bulk of the massive main-sequence galaxy population (Förster Schreiber & Wuyts 2020), which commonly feature central compact bulges and accreting black holes, galactic winds, and giant star-forming complexes on kpc scales (Genzel et al. 2011, 2014; Wuyts et al. 2012, 2013; Lang et al. 2014; Tacchella et al. 2018; Förster Schreiber et al. 2018, 2019; Ferreira et al. 2023; Espejo Salcedo et al. 2025b; Kalita et al. 2025). Star-forming galaxies at $z \approx 2$ represent a perfect laboratory to probe how galaxies grow and self-regulate, and to investigate the origin of the tight scaling relations between the global properties of star-forming galaxies, observed in the local Universe and up to high redshift (e.g., Speagle et al. 2014; Maiolino & Mannucci 2019).

Although observations with the *James Webb Space Telescope* (JWST) have mostly focused on the $z > 4$ Universe, leading to new extraordinary discoveries but also opening new questions (e.g., Finkelstein et al. 2023; Curtis-Lake et al. 2023; Carniani et al. 2024; Naidu et al. 2025), cosmic noon remains the key epoch to explore if we want to ultimately address the processes driving galaxy evolution. Compared to $z > 4$, $z \approx 2$ has the great advantage of being a sweet spot for both JWST and ground-based near-IR integral-field unit (IFU) observations with adaptive optics (AO), such as SINFONI (Spectrograph for INtegral Field Observations in the Near Infrared; Eisenhauer et al. 2003) and its successor ERIS (Enhanced Resolution Imager and Spectrograph; Davies et al. 2023) at the Very Large Telescope (VLT). While near-IR AO-assisted IFU spectrographs can reach much higher spectral resolution ($R \approx 11000$ with VLT/ERIS), uniquely enabling a thorough study of gas kinematics via line emission, the broad wavelength coverage of JWST and its high sensitivity provide us with imaging and spectroscopy of galaxies at $z \approx 2$ over an unprecedented broad and continuous rest-frame UV to near-IR wavelength range (Ferruit et al. 2022; Rieke et al. 2023). This gives us access to a wealth of interstellar medium (ISM) and stellar population properties (e.g. metallicity, dust extinction, ionisation state, stellar mass). Moreover, thanks to their high spatial resolution (∼ 0.1″), both facilities can probe physical scales down to ∼ 1 kpc, which is the typical Toomre scale (Toomre 1964), the fundamental scale governing gravitational instabilities in gas-rich rotationally supported galactic disks at $z \approx 1-3$ (e.g. Genzel et al. 2011). Therefore, by exploiting the

⋆ These authors contributed equally to this work.

synergy between JWST and ground-based AO IFU facilities, it is now possible to obtain a full picture of galaxies at cosmic noon, including gas kinematics, stellar properties, and ISM conditions (Park et al. 2024; Ju et al. 2025; Nestor Shachar et al. 2025; Slob et al. 2025).

In this work, we present JWST observations of K20-ID7 (GS4_29868; RA = 03:32:29.1, Dec = –27:46:28.5), a star-forming main-sequence galaxy ($M_\star \approx 4\times10^{10}$ $M_\odot$; Förster Schreiber et al. 2018) at $z = 2.224$, featuring a large, well-defined spiral morphology. This galaxy is the perfect laboratory to investigate many of the key mechanisms taking place at cosmic noon, from bulge growth and settling of morphological features, to star formation in kpc-scale clumps, and radial gas transport. Being located in GOODS-South, one of the most targeted extragalactic fields, K20-ID7 has a plethora of observations from both large space surveys and deep dedicated ground-based follow-ups. It was indeed extensively observed from space with the *Hubble Space Telescope* (HST), as part of the GOODS (Great Observatories Origins Deep Survey, Giavalisco et al. 2004), CANDELS (Cosmic Assembly Near-Infrared Deep Extragalactic Legacy Survey, Grogin et al. 2011; Koekemoer et al. 2011) and 3D-HST (Brammer et al. 2012; Skelton et al. 2014) surveys, and also at longer wavelengths with *Spitzer* (Dickinson et al. 2003; Ashby et al. 2013; Whitaker et al. 2014) and *Herschel* (Lutz et al. 2011). It also benefits from deep ground-based AO-assisted IFU observations at high spectral and spatial resolution. The first deep high-resolution IFU data were obtained with VLT/SINFONI, as part of the AO SINS/zC-SINF survey (Förster Schreiber et al. 2018), where the Hα kinematics revealed a globally ordered velocity field compatible with disk rotation (Förster Schreiber et al. 2018; Espejo Salcedo et al. 2025a), and provided evidence for radial gas inflows along a spiral arm (Genzel et al. 2023). More recently, K20-ID7 has been followed up with VLT/ERIS at superior spectral ($R \approx 10500$) and spatial resolution, within the Guaranteed Time Observations (GTO) program GALPHYS (PI: N. M. Förster Schreiber). The detailed Hα kinematics and morphology traced in ERIS data has enabled a thorough study of kpc-scale star-forming clumps (Förster Schreiber et al. in prep.), and a robust characterization of gas inflows (Pulsoni et al., in prep.).

For galaxies at $z \sim 2$, JWST data allow for continuous coverage from the rest near-UV to the rest near-IR. K20-ID7 has a wealth of archival JWST spectroscopy and imaging. These data are from the GTO JWST Deep Extragalactic Survey (JADES, Eisenstein et al. 2023) in the *Hubble* Ultra Deep Field (HUDF) and surrounding GOODS-South (Bunker et al. 2024), and from the Cycle 1 General Observer (GO) program FRESCO (First Reionization Epoch Spectroscopically Complete Observations; Oesch et al. 2023).

In this work, we leverage the rich dataset available for K20-ID7 to present a complete characterization of its ISM conditions and stellar properties on scales down to ~ 1 kpc, and thus gain insights into its formation and evolution mechanisms. The paper is structured as follows. In Sect. 2 we present all the data analyzed in this work, including from JWST, but also from HST/ACS and ALMA, and provide details on the data reduction. In Sect. 3, we infer local ISM properties for the different galaxy regions covered by distinct MSA shutters, whereas Sects. 4 and 5 are respectively dedicated to the resolved SED fitting of NIRCam and HST imaging, and to spatially mapping star formation via Paβ in NIRCam WFSS data. The resolved results are then also compared with those from integrated SED analysis, also including available mid- and far-IR photometry. In Sect. 6, we discuss the inferred results in the context of possible scenarios of galaxy growth and evolution, and in Sect. 7 we draw our conclusions.

Throughout this work, we use the following notation to refer to key emission-line diagnostics:

- R2 = log([OII]$\lambda\lambda$3726,29/Hβ)
- R3 = log([OIII]λ5007/Hβ)
- O3O2 = R3 – R2
- N2 = log([NII]λ6584/Hα)
- O3N2 = R3 – N2
- N2O2 = log([NII]λ6584/[OII]$\lambda\lambda$3727,29)
- S2 = log[([SII]λ6716 + [SII]λ6731)/Hα]
- S23 = log[([SII]$\lambda\lambda$6716,31 + [SIII]$\lambda\lambda$9069,9533)/Hβ]
- N2S2 = log([NII]λ6584/[SII]$\lambda\lambda$6716, 31).

We adopt the cosmological parameters from Planck Collaboration et al. (2016): $H_0 = 67.7$ km s^{-1} Mpc^{-1}, $\Omega_m = 0.307$, and $\Omega_\Lambda = 0.691$ and a Chabrier initial mass function (Chabrier 2003).

2. Data

In this section, we present all data employed in this paper, mostly from JWST, but also from HST (ACS images in 5 filters) and ALMA (Band 6 continuum at 1.2 mm), along with the data reduction. The JWST data consist of: NIRCam imaging in 11 filters; NIRSpec MSA spectra at $R \sim 100$, $R \sim 1000$, and $R \sim 2700$; and NIRCam WFSS F444W data ($R \sim 1600$).

2.1. JWST/NIRCam and HST/ACS imaging

K20-ID7 was recently observed as part of the JADES survey (Eisenstein et al. 2023) in the Hubble Ultra Deep Field (Bunker et al. 2024), which acquired NIRCam imaging in 11 different broad- and medium-band filters (F090W, F115W, F150W, F182M, F200W, F210M, F277W, F335M, F356W, F410M, F444W), and NIRSpec MSA spectroscopy (presented in Sect. 2.2). Additional NIRCam data also come from the Cycle 1 FRESCO survey (PI: P. Oesch, program ID: 1895; Oesch et al. 2023), a NIRCam WFSS program that obtained grism spectroscopy (see Sect. 2.3) and imaging in the F444W, along with parallel imaging in the medium-band F182M and F210M filters. Among HST imaging available, we only use publicly released HST/ACS imaging (F435W, F606W, F775W, F814W, F850LP) from the GOODS and CANDELS surveys (Giavalisco et al. 2004; Grogin et al. 2011; Koekemoer et al. 2011), and discard the WFC3/IR images, since they cover the same wavelengths as the bluer NIRCam filters, yet at lower sensitivity and spatial resolution.

For five NIRCam filters (F182M, F210M, F277W, F356W, F444W), we adopt the high-quality reductions publicly released on the DAWN JWST Archive[1] (DJA). These were obtained using the `grizli`[2] reduction software (Brammer 2019, 2023), which performs standard calibrations, astrometric alignment with `DrizzlePac`[3], and background subtraction optimized to preserve faint emission and to minimize the noise. Since the reductions of the NIRCam images in the other six filters (F090W, F115W, F150W, F200W, F335M, F410M) have not yet been publicly released on DJA, we retrieve the uncalibrated NIRCam data from the Mikulski Archive for Space Telescopes (MAST) portal[4], and reduce them using a custom-made reduction pipeline (see Espejo Salcedo et al. 2025b for a detailed description of the pipeline). This reduction exploits the

[1] https://dawn-cph.github.io/dja/
[2] https://github.com/gbrammer/grizli
[3] https://www.stsci.edu/scientific-community/software/drizzlepac
[4] https://archive.stsci.edu/

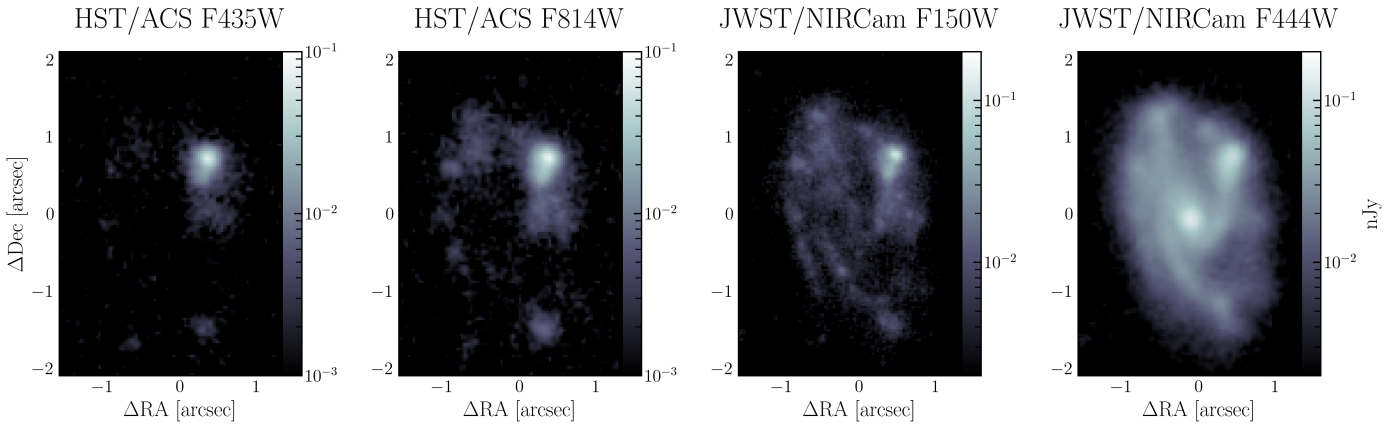

Fig. 1. Images of K20-ID7 in four representative HST/ACS (F435W, F814W) and JWST/NIRCam (F150W, F444W) filters, tracing galaxy emission from rest-frame UV to near-IR wavelengths. Redder NIRCam imaging unambiguously reveals a regular, unperturbed galaxy morphology, with well-defined spiral arms, and a compact bulge which appears brighter in the reddest F444W filter. All images are in units of nJy.

CrabToolkit[5], which follows the standard JWST image processing steps[6], and also applies additional steps to improve the removal of artifacts through a combination of manual masking and publicly available templates[7]. The reduced images are then astrometrically corrected, furthermore improved with an additional flat background subtraction, and finally produced with a 0.025″ pixel scale and aligned with North up and East left, consistently with DJA reductions. Similarly, we also produce HST images with the same North-East orientation and 0.025″ pixel sampling.

Figure 1 displays four representative HST/ACS (F435W and F814W) and JWST/NIRCam (F150W and F444W) images of K20-ID7, each showing the morphology of the galaxy emission at different wavelengths, spanning the rest-frame UV to near-IR. The comparison between JWST/NIRCam and HST/ACS images immediately highlights how crucial it is to cover redder wavelengths with JWST/NIRCam in order to get a complete, unambiguous view of this galaxy. Moving to redder wavelengths, spiral arms stand out in sharp relief, as well as a compact red bulge gradually appears, which becomes particularly bright and evident in the reddest F444W filter. A first composite-color image of K20-ID7 including NIRCam F444W band was presented in Genzel et al. (2023), which revealed for the first time the large outstanding spiral and central red bulge of this galaxy.

2.2. NIRSpec MSA spectroscopy

In addition to NIRCam imaging, the JADES survey also acquired deep NIRSpec MSA spectroscopy of targets in the HUDF and surrounding GOODS-South field at low ($R \sim 100$, with PRISM/CLEAR), medium ($R \sim 1000$, with G140M/F070LP, G235M/F170LP, and G395M/F290LP), and high resolution ($R \sim 2700$, with G395H/F290LP). In particular, the NIRSpec/MSA data of K20-ID7 were obtained as part of the JADES program 1210 (PI: N. Lützgendorf), and consist of two distinct datasets associated to different pointings (Fig. 2, left panel). The two pointings were centered on the two UV blue bright clumps, visible in the HST/ACS imaging (see Fig. 1), which were indeed classified as two separate entries (i.e. two distinct galaxies) in the CANDELS and 3D-HST catalogs (Skelton et al. 2014).

The NIRSpec/MSA data of K20-ID7 were publicly released as part of the first JADES data release (Bunker et al. 2024), along with a public reduced version of the spectra obtained using the NIRSpec MSA GTO pipeline (Scholtz et al. 2025). This performs a point-source pathloss correction and a local background subtraction, by measuring the background in lateral shutters, and subtracting it from the 'science' spectrum from the central shutter. While this standard procedure has widely proven to work well for compact sources (e.g., more distant galaxies at $z > 4$, Bunker et al. 2024), it is not suitable for extended sources like K20-ID7, where the side shutters are also placed on emitting regions of the galaxy. Therefore, if used to measure the background, they lead to a self-subtraction of line and continuum emission. Moreover, it is important to apply an accurate pathloss correction in order to properly account for both geometric losses due to galaxy light partially falling out of the micro-shutter mask and diffraction losses, as a consequence of light lost across the NIRSpec optical path. The standard pipeline performs a reliable pathloss correction either in the case of a point-like source, or if the micro-shutter is uniformly illuminated. Since the MSA data of K20-ID7 match none of these options, the standard pathloss correction used in the public reduced data is likely to have produced incorrect fluxes, and to have also altered the global spectral shape, because of the wavelength dependence of the pathloss correction.

For all these reasons, in this work we implement a custom reduction of the NIRSpec/MSA spectra of K20-ID7, which: i) performs an improved background subtraction and pathloss correction; ii) extracts science spectra from all MSA shutters that show galaxy emission. In the following, we describe the main steps of our adopted reduction procedure. We retrieve the count rate data from the MAST archive, and from these we extract the 2D trace of each spectrum for each visit, apply the wavelength calibration and flat-field correction, skipping the pathloss correction and background subtraction steps. After rectifying the 2D traces, we end up with the 2D rectified spectra relative to each grating/filter configuration, nod, and exposure.

By visually inspecting the resulting 2D rectified spectra, we find galaxy emission to be detected in the majority of the MSA shutters in the PRISM/CLEAR configuration (seven in total, the coloured shutters in the right panel of Fig. 2), and therefore create a *master* background, to remove from each shutter spectrum,

[5] https://github.com/1054/Crab.Toolkit.JWST
[6] https://jwst-docs.stsci.edu/jwst-science-calibration-pipeline/stages-of-jwst-data-processing
[7] https://jwst-docs.stsci.edu/depreciated-jdox-articles/nircam-claws-and-wisps

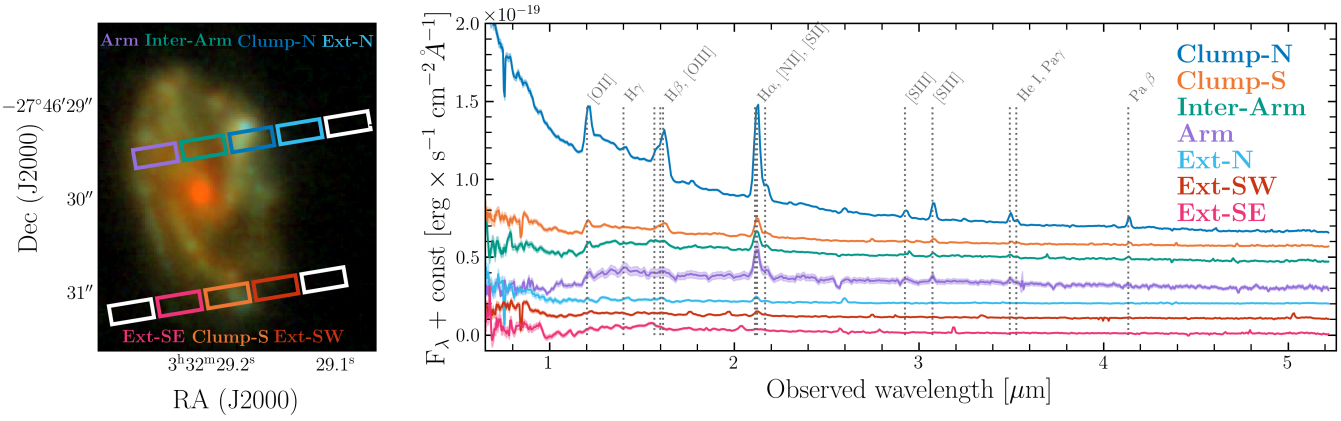

Fig. 2. NIRSpec MSA spectroscopy of K20-ID7. *Left*: Location of the two distinct MSA mask arrays, with open shutters drawn on the top of a NIRCam RGB image of K20-ID7, composed of F356W+F444W (red), F182M+F200W+F277W (green), and F090W+F115W+F150W (blue) filters. *Right*: PRISM/CLEAR spectra extracted from the seven coloured MSA shutters (those exhibiting some galaxy emission, same colors as in the left panel), using our custom-made reduction (described in Sect. 2.2). White shutters do not contain any galaxy emission. Spectra from different regions clearly differ in continuum shape and line intensities, over the total covered rest-frame near-UV to near-IR wavelength range. For the purpose of a better visualization, each spectrum has been vertically shifted by an arbitrary constant.

via the following procedure. By means of the MSA pipeline, we reduce the data relative to the same visit from all the shutters that were left open in the MSA mask on specifically selected source-free regions, and create the corresponding rectified background 2D spectra. For each visit, we then generate a unique 2D master background, computed as the median of the 2D rectified background spectra, and remove it from the 2D rectified science spectra previously obtained for K20-ID7. By combining all 2D background-subtracted spectra of K20-ID7, we thus obtain the final 2D PRISM spectra for each visit, from which we extract the 1D spectra relative to each shutter using a 5-pixel wide slit. We also adopt the same procedure for the 'error' extension of the observed data. For medium- and high-resolution data instead, we follow a different procedure for background subtraction, since galaxy emission is detected in fewer shutters (i.e., five shutters) compared to the PRISM/CLEAR configurations. In particular, since we do not detect galaxy emission in the light blue and pink shutters shown in the left-hand panel of Fig. 2, as opposed to the PRISM data, we use them to separately measure the background relative to each pointing. From these two background shutters, we therefore extract 1D background spectra using a 5-pixel wide slit, and subtract them from the 1D science spectra extracted from the other shutters of the same visit, thus obtaining medium- and high-resolution spectra for four distinct regions of K20-ID7. We note that, with this approach, we expect an effect of self subtraction on the Hα flux at most of $\sim 10\%$, while it is negligible for other emission lines.

Finally, to correct all MSA spectra for pathlosses, we measure the flux in the NIRCam images available for K20-ID7 from the region encompassed by each shutter, and use these flux values to re-scale the NIRSpec/MSA spectra via a linear fit to the ratio of the observed NIRCam fluxes to the observed NIRSpec/MSA counterparts in each shutter.

In summary, with our custom MSA reduction, we obtain in total seven PRISM/CLEAR spectra (see Fig. 2), and five spectra for each medium- and high-resolution grating/filter configuration. All together these spectra probe seven distinct galaxy regions: clumps (labelled as Clump-N and Clump-S), spiral arm (Arm), inter-arm (Inter-Arm), and more external diffuse regions (Ext-N, Ext-SW, Ext-SE). Both low-resolution PRISM ($R \sim 100$) and all medium-resolution spectra ($R \sim 1000$) cover a total spectral range from 0.6 μm to 5.2 μm, corresponding to rest-frame near-UV to near-IR wavelengths at $z \sim 2$. High-resolution observations ($R \sim 2700$) have instead only been obtained with the reddest grating (i.e. G395H/F290LP), and are therefore limited to the wavelength range 2.9 – 5.2 μm, encompassing the rest-frame near-IR emission of K20-ID7. Details on the covered wavelength range, the spectral resolution, and the exposure time relative to each MSA grating/filter configuration are summarized in Table 1. The exposure time reported refers to the central shutter of each array; the exposure time decreases to 2/3 and 1/3 at increasing distance from the central shutter.

Table 1. NIRSpec/MSA observations of K20-ID7 used in this paper.

Dataset	$\Delta\lambda$ [μm]	R	$t_{\rm exp}$ [ks]
PRISM/CLEAR	0.6 – 5.3	30 – 300	33.6
G140M/F070LP	0.7 – 1.9$^{(\star)}$	500 – 890	8.4
G235M/F170LP	1.7 – 3.2	720 – 1340	8.4
G395M/F290LP	2.9 – 5.2	730 – 1315	8.4
G395H/F290LP	2.9 – 5.2	1930 – 3615	8.4

Notes. Wavelength coverage, nominal spectral resolution (Ferruit et al. 2022), and exposure time of the observations in each distinct grating/filter configuration. The $t_{\rm exp}$ reported refers to the central shutter for each visit. $^{(\star)}$The nominal wavelength range is 0.7 – 1.3 μm, but as done in JADES (Bunker et al. 2023), we recover the spectrum up to 1.9μm, effectively acting as G140M/F070LP+F100LP.

2.3. NIRCam WFSS data

In this work, we use JWST/NIRCam WFSS F444W observations of K20-ID7 from FRESCO (Oesch et al. 2023), obtained with an exposure time of 7 ks, which consist of grism spectra over the range 3.8 – 5.0 μm at a spectral resolution of $R \sim 1600$, covering rest near-IR wavelengths at $z \sim 2$. Slitless spectra of K20-ID7 were acquired with a 90° position angle of the grism dispersion axis (i.e. WE aligned, with increasing wavelengths towards E). All FRESCO NIRCam WFSS data, including those

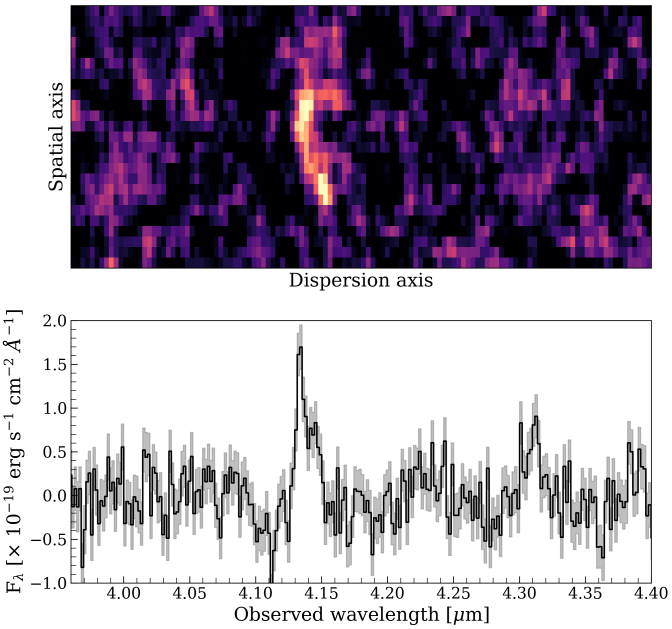

Fig. 3. Continuum-subtracted NIRCam F444W WFSS data of K20-ID7, zoomed-in over 3.95 – 4.40 μm, encompassing Paβ line emission. In the 2D slitless spectra (upper panel), Paβ line emission is clearly spatially resolved perpendicularly to the dispersion axis, and also extended along the parallel direction, which leads to a double-peaked Paβ line profile in the total 1D spectrum (lower panel). This is consequence of resolved spatial offsets combined with velocity gradients along the grism dispersion axis (discussed in Sect. 5).

of K20-ID7 used in this work, were reduced using the publicly available `grizli` code (Brammer et al. 2012; Brammer 2023). Continuum-subtracted spectra were then produced by running a median filter along each row of the 2D grism spectra, adopting a 12-pixel central gap in the filtering to minimise line self-subtraction (Kashino et al. 2023). For further details on the observational design and reduction of FRESCO observations, we refer the reader to the main papers of the survey (e.g. Oesch et al. 2023; Nelson et al. 2024; Neufeld et al. 2024).

As shown in Fig. 3, the continuum-subtracted spectra of K20-ID7 clearly exhibit Paβ line emission detected at a total S/N = 19, and no additional emission lines are detected. Compared to optical Balmer emission lines (e.g. Hα and Hβ), near-IR Paschen lines are less affected by dust attenuation, and therefore can probe recent ($\sim$ 10 Myr) star formation in a more obscured regime. In the 2D slitless spectra (upper panel), Paβ appears to be spatially resolved along the spatial axis (i.e. perpendicularly to the grism dispersion axis), and also extended along the spectral axis, resulting in a double-peak Paβ line profile in the total 1D spectrum (lower panel). As later addressed in Sect. 5, this is a consequence of real spatial offsets combined with velocity gradients along the grism dispersion axis.

2.4. ALMA data

We reduce the available ALMA Band 6 1.2 mm continuum data (PI: J. Scholtz, program ID 2018.1.01044.S) using `CASA`. We retrieve the raw visibilities from the ALMA archive, and calibrate them by executing the script delivered with the data. We then clean the data by using the task `tclean` in `CASA`, and image them using natural weighting and a pixel scale of 0.1" to obtain the best sensitivity. The final continuum image has an angular resolution of 0.5″×0.6″. Finally, we create a segmentation map using the `python` package `photutils.psf.matching` to isolate the continuum flux of the galaxy from neighbours, by using a threshold of twice the noise level, and sum over the masked pixels. We thus obtain a 1.2 mm continuum flux of 0.36 ± 0.11 mJy.

3. Local ISM properties from spectroscopy

The wavelength range covered by the NIRSpec MSA data ($\sim$ 0.7 – 5.2 μm) encompasses several emission lines, we use to infer the properties of the galactic ISM by means of various emission-line diagnostics. In particular, we infer nebular dust attenuation, the ionisation parameter, electron density ($A_{V,\rm neb}$, log(U), $n_{\rm e}$), and chemical abundances (O, N, S) for the galaxy regions where the key emission lines are detected at S/N > 3. In Appendix A, we describe the spectral fitting of the MSA spectra, and summarise the best-fit results. For the shutters having the same emission lines detected with more than one spectral setup, we adopt as fiducial line fluxes those obtained from the medium-resolution data: these have a higher S/N compared to the high-resolution data, and close emission lines (e.g. Hβ + [OIII], Hα + [NII], [SII] line doublet) well separately resolved, unlike in the PRISM data. Therefore, when available, we only combine the medium-resolution line fluxes to derive ISM properties, thus also avoiding issues due to a possible inaccurate absolute flux calibration (D'Eugenio et al. 2025).

3.1. Dust attenuation, ionisation, and electron density

The first important physical property to derive is the (nebular) dust attenuation ($A_{V,\rm neb}$), which allows us to correct all observed line fluxes, to then measure the other ISM properties. Within the broad spectral range covered by the NIRSpec MSA data of K20-ID7, there are several hydrogen emission lines (i.e., Hδ, Hγ, Hβ, Hα, Paγ, Paβ), which can be used to infer multiple measurements of $A_{V,\rm neb}$ from distinct line ratios. In Table 2, we report the $A_{V,\rm neb}$ measurements that we derive by combining the highest-S/N hydrogen lines (i.e. Hβ, Hα, Paβ, when detected), by assuming a Calzetti et al. (2000) dust attenuation law and adopting theoretical line ratios of 2.86, 0.0569, 0.163, as predicted for warm ionised gas ($T = 10^4$ K; Osterbrock & Ferland 2006) for Hα/Hβ, Paβ/Hα and Paβ/Hβ, respectively. For the Inter-Arm region, we derive $A_{V,\rm neb}$ from the Paβ/Hα ratio only, since we have no measurement of the Hβ flux in this shutter[8]. For the clump regions (Clump-N and Clump-S), where we detect all three hydrogen lines, we obtain consistent measurements of $A_{V,\rm neb}$ from different hydrogen line ratios within 2σ. Small differences in the derived A_V using different line ratios might be due to the different shape of attenuation curves at high redshift (Markov et al. 2025) compared to local ones. To verify this, we also compute $A_{V,\rm neb}$ by adopting the high-z attenuation curve by Reddy et al. 2025, finding values comparable within the uncertainty with our estimates reported in Table 2. In the rest of this section, we adopt as fiducial values the weighted average between the available measurements for each region that we report in Table 2[9]. For the Arm region, Hα is the only hydrogen line being detected and, therefore, we cannot estimate $A_{V,\rm neb}$. However, this is not crucial,

[8] For the Inter-Arm region, Hβ is only detected in the PRISM spectrum, but here appears blended with [OII]$\lambda\lambda$5007,4959. Therefore, it cannot be disentangled.

[9] For Clump-S we only consider the two inferred $A_{V,\rm neb}$ estimates, hence we exclude the upper limit inferred from Hα/Hβ.

Table 2. ISM properties inferred from NIRSpec MSA spectra from the three higher-S/N shutters of K20-ID7.

Diagnostic	Arm	Inter-Arm	Clump-N	Clump-S
		$A_{V,\rm neb}$ [mag]		
Hα/Hβ	-	-	$0.6^{+0.1}_{-0.1}$	<0.9
Paβ/Hα	-	$1.3^{+0.4}_{-0.5}$	$0.2^{+0.1}_{-0.1}$	$0.6^{+0.4}_{-0.6}$
Paβ/Hβ	-	-	$0.4^{+0.1}_{-0.1}$	$0.3^{+0.3}_{-0.4}$
Fiducial	-	$1.3^{+0.4}_{-0.5}$	$0.4^{+0.1}_{-0.1}$	$0.4^{+0.3}_{-0.3}$
		$n_{\rm e}$ [cm^{-3}]		
[SII]	-	< 1900	260^{+120}_{-139}	< 310
		log(U)		
[SII], [SIII]	-	$-3.3^{+0.3}_{-0.2}$	-3.05 ± 0.05	-3.0 ± 0.2
[OII], [OIII]	-	$-3.1^{+0.3}_{-0.5}$	-2.97 ± 0.02	-3.1 ± 0.1
Fiducial	-	-3.3 ± 0.3	-3.01 ± 0.03	-3.1 ± 0.2
		12+log(O/H)		
Fiducial	$8.57^{+0.20}_{-0.21}$	$8.58^{+0.06}_{-0.06}$	$8.49^{+0.06}_{-0.06}$	$8.51^{+0.08}_{-0.08}$
		log(N/O)		
N2O2	-	-0.8 ± 0.2	-0.95 ± 0.05	-1.1 ± 0.1
N2S2	-	-0.9 ± 0.2	-0.95 ± 0.10	-1.2 ± 0.2
Fiducial	-	-0.9 ± 0.2	-0.95 ± 0.08	-1.2 ± 0.2
		12+log(S/H)		
S23	-	$6.6^{+0.2}_{-0.2}$	$6.6^{+0.2}_{-0.2}$	$6.7^{+0.3}_{-0.2}$
		log(S/O)		
	-	-2.0 ± 0.2	-1.9 ± 0.2	-1.8 ± 0.3

Notes. From the top: nebular attenuation $A_{V,\rm neb}$, derived from different hydrogen line ratios (Calzetti et al. 2000); electron density $n_{\rm e}$ from the [SII] line ratio (Sanders et al. 2016); ionisation parameter log(U) using sulfur- and oxygen based diagnostics (Díaz et al. 2000); gas phase metallicity (12+log(O/H)) inferred by combining various strong-line diagnostics (Sanders et al. 2025); log(N/O) abundance (Hayden-Pawson et al. 2022); 12+log(S/H) abundance (Díaz & Zamora 2022); log(S/O) abundance, inferred by combining the 12+log(S/H) value with the fiducial 12+log(O/H) one. All upper limits correspond to 2σ.

since [NII] and Hα are the only emission lines detected in this region, and therefore we can only infer the [NII]/Hα emission-line diagnostic (used in Sect. 3.3 to derive metallicity), for which dust extinction is negligible, given the proximity in wavelength of these lines. We reiterate that the $A_{V,\rm neb}$ values inferred in this section from hydrogen line ratios refer to nebular dust attenuation, which might be higher than the attenuation affecting stellar continuum ($A_{V,\rm star}$ inferred from SED modeling in Sect. 4), since HII regions are typically more embedded in dust.

Following Sanders et al. (2016), we then measure $n_{\rm e}$ from the dust-corrected [SII]$\lambda\lambda$6716, 31 line doublet. For Clump-N, we find an electron density of $n_{\rm e} \simeq 260$ cm^{-3}, consistent with typical values inferred for $z \approx 2$ star forming regions (Sanders et al. 2016; Davies et al. 2021; Topping et al. 2025). Unfortunately, the [SII] λ6717/λ6731 ratio for the other two regions (i.e., Clump-S and Inter-Arm) yields non-physical (negative) values of $n_{\rm e}$, therefore, we adopt for them a conservative 2σ upper limit.

Given the high sensitivity and the wide wavelength coverage of the NIRSpec/MSA spectra of K20-ID7, for each high-S/N galaxy region, we derive two independent measurements of the ionization parameter from [OII]/[OIII] and [SII]/[SIII] line ratios, respectively. The [SIII]λ9069 emission line is detected in the medium resolution grating only in the Clump-N spectra. However, we can estimate it for the Inter-Arm and Clump-S regions, from the dust-corrected flux of the [SIII]λ9533 line measurement available by assuming a theoretical ratio of [SIII]λ9533/[SIII]λ9069 = 2.61 (Osterbrock & Ferland 2006). We note that for Clump-S we have a measurement of the [SIII]λ9069 from the PRISM spectrum, but the majority of the PRISM data are affected by a bad feature nearby that emission line (see Fig. A.1). Finally, we obtain a dust-corrected flux of [SIII]λ9069 of $\sim 2.7 \times 10^{-19}$ erg s^{-1} cm^{-2} and 3.2×10^{-19} erg s^{-1} for the Inter-Arm and Clump-S regions, respectively. Using the [OII]/[OIII]- and [SII]/[SIII]-based calibrators from Díaz et al. 2000, we thus infer two independent values of log(U) for each region. All inferred measurements point to log(U) $\simeq -3.0$ in both Clump-N and Clump-S, and a similar value but with larger uncertainties for the Inter-Arm region. This value is small, although consistent with what is found for other high-z galaxies (Reddy et al. 2023a).

3.2. Gas phase metallicity

In this work, we use metallicity calibrations from Sanders et al. (2025), based on six distinct diagnostics, namely R2, R3, O32, N2, O3N2 and S2 (see the end of Sect. 1 for all definitions). For the Inter-Arm region, where we had no direct flux measurement of the Hβ emission lines needed for four diagnostics), we estimate the Hβ flux from our fiducial dust-extinction corrected Hα flux (i.e. measured from medium-resolution data and corrected for $A_{V,\rm neb} = 1.3^{+0.4}_{-0.5}$, see Table 2), assuming a theoretical Hα/Hβ line ratio of 2.86 (Osterbrock & Ferland 2006). We thus obtain an Hβ flux of 2.75×10^{-17} erg s^{-1} cm^{-2} for the Inter-Arm region. In the Arm region, we only use N2, since Hα and [NII] are the only detected emission lines.

Following an approach similar to that described in Curti et al. 2020a, we derive the metallicity that minimizes simultaneously the χ^2 between the observed line ratios and the expected value according to each calibrator, by using the `python` library `lmfit`. The resulting best-fit metallicity values along with their error (also accounting for the intrinsic scatter of the calibrators) are reported in Table 2. We find no statistically significant difference in metallicity between the various regions, with consistent values within the uncertainty that indicate slightly subsolar metallicities $12 + \log(\rm O/H) = 8.49 - 8.58$ (i.e. $\sim 0.60 - 0.80\, Z_\odot$[10]). Nonetheless, it is interesting that the star-forming clumps, where newborn stars are expected to inject metals into the ISM, do not show a higher metallicity compared to the other regions. We speculate that any more prominent intrinsic difference (if present) might indeed result in being smoothed due to the spatial extent of the shutters, which encompass the emission from physically different regions. Indeed, the Clump-N shutter is not perfectly centered on the clump, and the Inter-Arm one might be contaminated from the emission of the clump close by (see Fig. 2). Interestingly, all the derived metallicities are consistent with what expected from the Fundamental Metallicity Relation (FMR; Mannucci et al. 2010) for K20-ID7, given its stellar mass and star formation rate (SFR; $M_\star \approx 4 \times 10^{10}$ M$_\odot$ and SFR ≈ 120 M$_\odot$ yr^{-1}, inferred later in Sects. 4 and 5). By using the parametrization by Curti et al. (2020b), the FMR predicts a gas phase metallicity $12 + \log(\rm O/H) \approx 8.57$. As will be discussed in Sect. 6.2, this finds

[10] We assume a solar metallicity $12 + \log(\rm O/H)_\odot = 8.69$ (Asplund et al. 2021).

connection with the presence of gas inflows (Genzel et al. 2023; Pulsoni et al., in prep.).

3.3. Chemical abundances: N/O, S/H, S/O

Among chemical elements, nitrogen is one of the most extensively studied, from the local Universe up to high redshift (Pilyugin et al. 2012; Shapley et al. 2015; Masters et al. 2016; Strom et al. 2018; Stiavelli et al. 2025; Sanders et al. 2025). In star-forming galaxies, its abundance can be derived from the relatively bright [NII] and [OII] emission lines, via the N2O2 diagnostic (e.g. Steidel et al. 2016; Strom et al. 2018; Hayden-Pawson et al. 2022). Since these lines originate from nearly the same ionization zones and have similar ionization potential, their ratio has little dependence on the ISM ionization conditions. As an alternative, one can infer N/O using the N2S2 diagnostic, which assumes the S/O abundance to be constant, and benefits from being less affected by dust extinction, since the lines involved are closer than [NII] and [OII] in N2O2. Yet, the [SII] emission lines have a lower ionization potential (10.4 eV), and therefore might be emitted from regions with softer radiation fields. Moreover, the assumption of a constant S/O abundance, necessary to use [SII] as a proxy for oxygen, may not always be true. For all these reasons, we provide two independent measurements of N/O in the various galaxy regions, adopting the calibrations from Hayden-Pawson et al. (2022) (see Table 2). For each region, N2O2- and N2S2 diagnostics deliver consistent values-based N/O values for each region; we adopt their average as fiducial value. The Clump-S has a N/O abundance 0.3 dex higher than the one in the Inter-Arm, with the Clump-N being between the two. We obtain similar results by also using the calibrations for N2O2 and N2S2 presented in Strom et al. (2018).

Similar to oxygen, sulfur is produced by massive stars and, therefore, the relative S/O abundance is expected to remain constant at about the solar value (i.e. $\log(\mathrm{S/O})_\odot = -1.57$; Asplund et al. 2021). The sulfur abundance $12+\log(\mathrm{S/H})$ has been studied only for a handful of galaxies at $z>1$ (e.g. Sanders et al. 2020; Rogers et al. 2024, 2025) and can be derived from the optical [SII] and [SIII] emission lines. Compared to the [OII] and [OIII] lines used to infer $12+\log(\mathrm{O/H})$, the sulfur lines have a milder (although still exponential) dependence on electron temperature, due to their lower ionisation potential, which makes them detectable even at solar or supersolar abundances (Díaz et al. 2007). For K20-ID7, we estimate $12+\log(\mathrm{S/H})$ from the S23 diagnostic (Díaz & Zamora 2022; see Table. 2). Interestingly, all the three examined galaxy regions consistently feature a subsolar S/H abundance ($12+\log(\mathrm{S/H})_\odot = 7.12$; Asplund et al. 2009), that is $12+\log(\mathrm{S/H}) \approx 6.6 - 6.8$. By finally combining these measurements of $12+\log(\mathrm{S/H})$ with our derived fiducial values of $12+\log(\mathrm{O/H})$, we estimate a relative log(S/O) abundance of about -1.9, consistent for all regions, which is systematically lower than the expected nearly constant (solar) value of -1.57 ± 0.05 (Asplund et al. 2021). In Sect. 6.3, we will investigate the implications of this result, discussing possible formation and depletion channels for sulfur.

4. Resolved SED fitting

In this section, we present spatially resolved SED modeling of high-resolution JWST/NIRCam and HST/ACS imaging to derive 2D maps of main galaxy physical properties (e.g., stellar mass and age, dust attenuation, SFR). We then compare the resolved results with those obtained from integrated SED fitting, also including low-resolution photometry at longer wavelengths, as well as with those inferred from NIRSpec MSA in Sects. 3.

4.1. PSF matching and SED modeling with CIGALE

We match all reduced $6'' \times 6''$ cutouts to the spatial resolution of the F444W band (FWHM = 0.15″). For JWST/NIRCam and HST/ACS data, we respectively use `WebbPSF` models and empirical PSFs from 3DHST (Skelton et al. 2014), to create F444W matching kernels through the `python` package `photutils.psf.matching`, and thus convolve each image to the F444W PSF. To estimate the background noise to adopt as error on pixel fluxes, also accounting for spatial correlations between pixels introduced by the data reduction, the PSF matching, and instrumental features, for each cutout we create a segmentation map and perform flux measurements in 100 randomly placed 'empty' apertures for a suite of aperture size with a variable linear size of N pixels (up to $N = 10$; see also Tacchella et al. 2015b). We thus derive the effective rms from the distribution of fluxes as a function of aperture size, and quantify the rms within one pixel. Since at a fixed aperture size, the effective rms is expected to be spatially constant, we adopt a constant flux error for all pixels of a given cutout.

To model the SED of individual pixels, we use the SED fitting code `CIGALE` (Boquien et al. 2019), and only fit the SED of pixels with S/N > 7 on the F444W band, based on the noise estimate inferred above. This adopted S/N threshold allows for a continuous mapping of the whole galaxy, and guarantees a S/N $\gtrsim 2$ in the bluer NIRCam filters, which indeed leads to good reduced χ^2 values ($\chi^2_{\mathrm{red}} \approx 1$) in the fit of individual pixels (see Fig. 4, bottom right panel). The SED of each S/N(F444W) > 7 pixel is then modeled independently from the other pixels under the same set of assumptions. For all pixels, we fix the redshift to $z = 2.224$ measured from Hα (Förster Schreiber et al. 2018), and assume a decaying exponential star formation history (SFH), allowing ages since the onset of star formation between 50 Myr and 2900 Myr (i.e. the age of the Universe at $z = 2.224$), and e-folding τ times from 10 Myr to 8000 Gyr (i.e. approximately corresponding to a constant SFH). We adopt Bruzual & Charlot (2003) stellar population synthesis models, assuming a Chabrier (2003) initial mass function, and fixing the metallicity to $Z = 0.008$[11], to reduce the number of free parameters and avoid degeneracy with other physical quantities. Such metallicity (corresponding to $\sim 0.4\,Z_\odot$) is slightly lower than what we inferred in Sect. 3.2. Yet, we find it to deliver better results compared to fixing metallicity to the solar value ($Z = 0.02$). In addition, we assume a Calzetti et al. (2000) attenuation law and include nebular emission, adopting suitable priors consistently with the ISM properties we inferred in Sect. 3, and simultaneously allowing for a large enough parameter space to also reproduce the properties of regions across the full system, possibly differing from those for which we have measurements from the MSA spectra. Among these, we set a two-value grid of n_e (100 cm^{-3} and 1000 cm^{-3}), and allow $\log(U)$ to vary from – 3.4 and – 2.0. With all these ingredients, our resolved SED modeling well reproduces the variety of single-pixel SED shapes, which reflect the intrinsic different nature and properties of distinct galaxy regions, such as clumps, spiral arm, and inter-arm regions (see Appendix B for representative examples of best-fit SEDs).

[11] `CIGALE` only allows for a limited choice of metallicity values, among which $Z = 0.008$ and $Z = 0.02$, with no intermediate value in between.

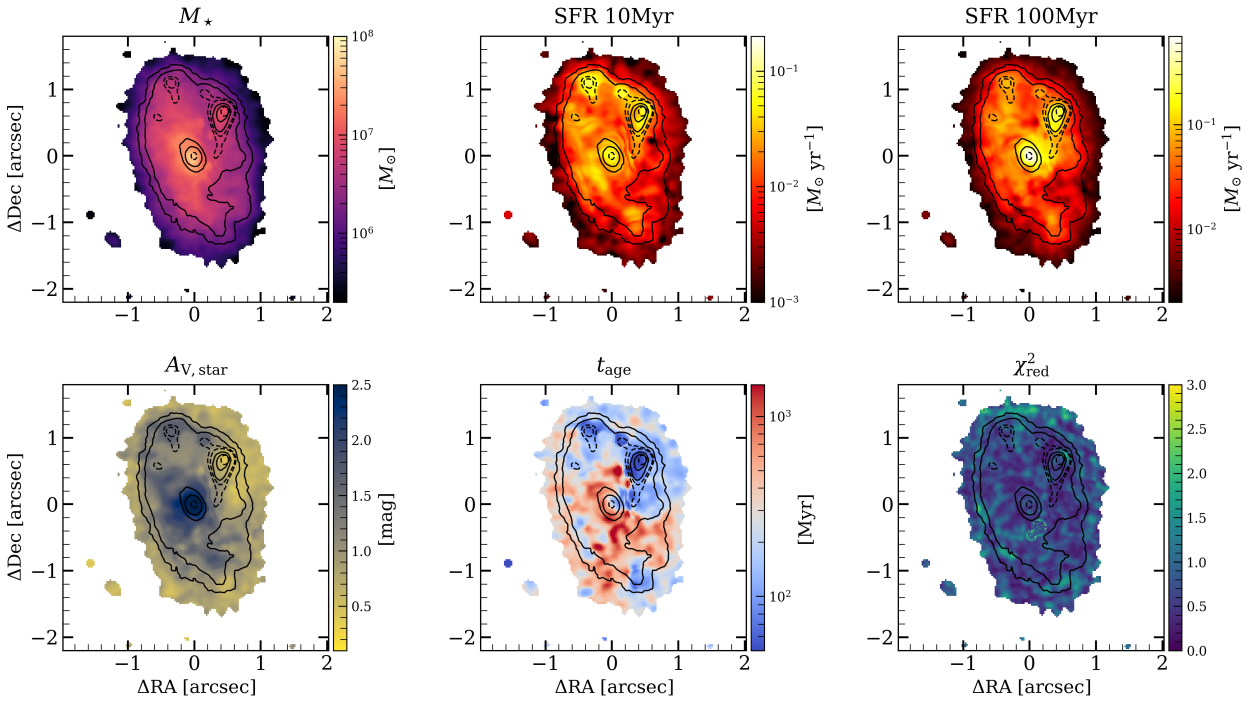

Fig. 4. 2D maps **at 25mas pixel scale** of the main galaxy properties, as resulting from our resolved SED fitting with CIGALE of HST/ACS and JWST/NIRCam images. From left to right, the top panels show maps of stellar mass, and SFRs averaged over the last 10 Myr and 100 Myr, while the bottom ones A_V, star, stellar age, and $\chi^2_{\rm red}$. The $\chi^2_{\rm red}$ map demonstrates the goodness of our pixel-by-pixel SED modeling, displaying values ~ 1 across the entire galaxy.

4.2. 2D maps of host galaxy properties

Figure 4 displays the resulting spatially resolved maps of relevant galaxy parameters, computed in CIGALE as the likelihood-weighted mean of the priors: stellar mass ($M_\star$), and the average SFRs computed over the last 10 Myr and 100 Myr in the top row (SFR10 and SFR100, respectively); stellar dust attenuation ($A_{V,\rm star}$), stellar age ($t_{\rm age}$), and reduced χ^2 in the bottom row. Table 3 summarizes the main physical properties for the most relevant regions (i.e., bulge and clumps), extracted using dedicated apertures (shown in Fig. 5 for a better visualization), and for the whole galaxy. In particular, for the bulge we adopt an aperture of 0.25″-diameter, corresponding to twice the bulge effective radius (i.e. $R_{\rm e,Bulge} \simeq 1$ kpc; Pulsoni et al., in prep.). As a consequence, all cumulative physical properties inferred hereafter for the bulge (i.e,. $M_\star$ and all SFRs) are computed by summing all values over the pixels within the bulge aperture, and multiplying by two the resulting sum value. The Clumps A and C roughly correspond to the regions covered by the Clump-N and Clump-S MSA shutters (see Fig. 2), respectively.

The most prominent feature in the stellar mass map is the central bulge ($M_{\star,\rm Bulge} = (7 \pm 3) \times 10^9$ M$_\odot$), which is then followed by the the brightest and largest star-forming Clump A ($M_{\star,\rm A} = (3.5 \pm 0.7) \times 10^9$ M$_\odot$). Given the resulting total galaxy stellar mass computed as the sum of all pixels ($M_\star = (3.7 \pm 1.0) \times 10^{10}$ M$_\odot$), we find that the bulge and the Clump A contribute by 19% and 9% to the total galaxy stellar mass, respectively. The SFR10 map follows well the clumps and the spiral arms, and reveals recent active star formation also in the central bulge (SFR10$_{\rm Bulge} = 12 \pm 8$ M$_\odot$ yr^{-1}). Averaging over a longer time frame, the SFR100 map displays a different morphology. Clump A has been forming stars intensely for the last 100 Myrs, while the spiral arms clearly underwent a weaker activity in the past. Interestingly, the bulge and its surroundings feature enhanced star formation over the last 100 Myr (SFR100$_{\rm Bulge} = 82 \pm 42$ M$_\odot$ yr^{-1}), suggesting that the bulge formed its stars mostly in the past.

In terms of dust extinction, the stellar attenuation map ($A_{V,\rm star}$) points to the highly obscured nature of the nuclear region ($A_{V,\rm star} = 2.83 \pm 0.24$). If we also account for extra attenuation of nebular line emission (i.e. $A_{V,\rm neb} \approx A_{V,\rm star}/0.44$; Calzetti et al. 2000), we infer a nebular attenuation $A_{V,\rm neb} = 6.43 \pm 0.55$. Significant extinction ($A_{V,\rm star} = 1.5 \simeq 2.0$) is also found in regions of intense star formation, such as along spiral arms, in Clump B, and in the surroundings of Clump A. The core of Clump A instead appears less attenuated ($A_{V,\rm star} \simeq 0.5$), consistently with the fact that it is also detected in the rest-frame UV.

Finally, the stellar age map highlights a relative trend as moving towards the inner galaxy regions, with younger stars ($t_{\rm age} = 50 - 100$ Myr) in the clumps, and older populations in the bulge and in the inter-arm regions ($t_{\rm age} \approx 400 - 2000$ Myr). The relatively older age of the bulge, combined with its enhanced SFR100, furthermore supports that it assembled most of its stellar mass in the past, with a current lower, but still present, star formation activity. An alternative opposite scenario might be that of a non-attenuated quiescent bulge, hosting extremely old stars and no recent star formation, which would still explain the observed red color of the bulge. To rule this hypothesis, we extract the integrated SED of the bulge using our adopted 0.25″ bulge aperture, and fit it with CIGALE following the same prescriptions as in Sect. 4.1 for the resolved SED fitting, but now with $A_{V,\rm star} = 0$. With this assumption, we obtain a poor best-fit ($\chi^2_{\rm red} = 12$), especially failing to reproduce the observed SED at redder wavelengths, where the observed slope is much steeper than the $A_{V,\rm star} = 0$ best-fit model, which flattens and does not reproduce most of the NIRCam photometry.

In Appendix D, we validate the results from our resolved SED fitting, showing that the 2D Hα distribution expected from

this fitting is in very good agreement with the observed ERIS Hα line map at similar angular resolution (Pulsoni et al., in prep.).

4.3. Integrated SED fitting

In this section, we perform SED modeling of integrated HST/ACS and JWST/NIRCam photometry, under the same assumptions as in Sect. 4.1, to compare the resolved results with the integrated ones. Results from this integrated SED fitting, including up to NIRCam F444W photometry, are summarised in Table 3 (see the column Galaxy$_{4.4\mu m}$; the best-fit model is shown in Appendix B).

Among all physical parameters, $M_\star$ is the most robustly constrained based on the available rest-frame optical HST/ACS and near-IR JWST/NIRCam photometry, while the other quantities would require to also cover longer mid- and far-IR wavelengths to constrain dust emission. As reported in Sect. 4.2, the total stellar mass of K20-ID7, computed as sum of all pixels, is $M_\star = (3.7 \pm 1.1) \times 10^{10}$ M$_\odot$. Such total value is slightly larger – by about a 1.6 factor, although consistent within the uncertainty – than the integrated result, that is $M_\star = (2.3 \pm 0.5) \times 10^{10}$ M$_\odot$. This difference likely reflects outshining effects by young stellar population, which leads to underestimated mass-to-light ratios in integrated SED modeling (e.g. Maraston et al. 2010; Wuyts et al. 2012; Giménez-Arteaga et al. 2023). Previous works (e.g. Sorba & Sawicki 2018; Giménez-Arteaga et al. 2023, 2024) found that stellar masses can indeed be underestimated up to a factor of five in integrated SED fitting, with larger offsets for higher specific SFR. In the case of K20-ID7, outshining seems to play a minor role, given the smaller discrepancy between the resolved and integrated result, which is more consistent with what found for star-forming galaxies of similar mass at $z \simeq 2$ (Shen et al. 2024) and at $z \simeq 4-6$ (Li et al. 2024; Lines et al. 2025).

In order to better constrain SFRs, stellar age and dust attenuation, we perform an additional integrated SED fitting, including the available photometry at longer wavelengths from *Spitzer* IRAC (5.8 μm and 8 μm) and MIPS 24 μm (Dickinson et al. 2003; Whitaker et al. 2014), *Herschel*/PACS 160 μm (Lutz et al. 2011) and ALMA Band 6 at 1.2 mm, introduced in Sect. 2.4. In `CIGALE`, we model dust emission by using dust templates of Dale et al. (2014) (see Appendix B for more details on the best-fit model).

As shown in Table 3 (see the column Galaxy$_{1.2mm}$), the inclusion of mid- and far-IR photometry leads to an excellent agreement of the integrated $M_\star$ value with the $M_\star$ sum over pixels, as well as to consistent $A_{V,\rm star}$ values. On the contrary, the inferred SFR10 and SFR100 values are systematically lower than those from both resolved SED fitting and integrated modeling with photometry up to 4.4 μm. In particular, the resulting SFR10 is lower than the other two inferred total SFR10 values, as well as than the most accurate values previously published in Förster Schreiber et al. (2009) (SFR = 101 – 190 M$_\odot$ yr^{-1}; see Sect. 5 for details on previously published SFRs). Yet, the wide coverage of this photometric dataset, extending up to far-IR, allows us to estimate the total SFR from the UV and IR luminosities of the SED best-fit model (Kennicutt 1998). In doing so, we obtain a higher SFR (SFR$_{\rm UV+IR} = 105 \pm 17$ M$_\odot$ yr^{-1}), consistent with the sum over pixels. Investigating the causes of the systematic lower SFR10 from the integrated SED analysis with photometry up to 1.2 mm goes beyond the purpose of this paper.

5. 2D spatial distribution of Paβ line emission

5.1. Correction of Paβ line map for velocity gradients

Compared to long-slit spectroscopy, slitless grism observations allow us to recover the overall 2D emission line distribution, after removing continuum emission (e.g. Nelson et al. 2016, 2024; Matharu et al. 2022). In particular, in case of grism data at high spectral resolution of extended sources, such as NIRCam WFSS ($R \sim 1600$, corresponding to a FWHM ≈ 190 km s^{-1}), the emission-line morphology along the dispersion axis is a combination of spatial and velocity displacements along this direction, unlike data at low spectral resolution (e.g. HST/WFC3 or JWST/NIRISS, $R \sim 100$, corresponding to a FWHM ≈ 2000 km s^{-1}), for which the dispersion axis contains spatial information only. As a consequence, accounting for this velocity-position degeneracy is a crucial, necessary step to recover the intrinsic 2D emission-line distribution or 1D line velocity profile from NIRCam WFSS data.

The left-hand panel of Fig. 5 shows the continuum-subtracted Paβ emission line map of K20-ID7, reconstructed by the FRESCO team using `grizli` (Brammer 2023; see Oesch et al. 2023; Neufeld et al. 2024 for more details on FRESCO reconstructed emission line maps), after being additionally matched to the spatial resolution of the VLT/ERIS AO-assisted data used later in this section (FWHM = 0.16″[12], against FWHM = 0.13″ of NIRCam F444W), by means of the `python` package `photutils.psf.matching`. The comparison with the continuum emission in the direct F444W image (white contours) clearly reveals a relative spatial offset with respect to Paβ line emission along the horizontal WE direction. Such offsets are fairly systematic and correspond to the expectations given the known observed kinematics and the orientation of the grism dispersion axis (increasing wavelengths towards E). K20-ID7 indeed features a kinematic position angle of 25 deg (i.e. roughly corresponding to the NE-to-SW direction), and a substantial velocity gradient (from -300 to +300 km/s; Förster Schreiber et al. 2018; Genzel et al. 2023, Pulsoni et al. in prep.), as seen in Hα kinematics from high-resolution IFU data. It follows that the largest offsets are observed at larger distances from the galaxy center along the kinematic major axis, where the velocity gradient is stronger. This can be well appreciated for the northernmost clump (i.e. Clump B, circled in red in the left and middle panels of Fig. 5). The fact that these offsets between continuum and line emission are not observed in VLT/ERIS Hα data furthermore supports their non-physical origin.

In order to break such spatial/kinematic degeneracy and recover the intrinsic Paβ spatial distribution, we rely on the (smoothed) Hα velocity map obtained from ERIS AO observations (Pulsoni et al., in prep.). Since Paβ and Hα emission originate from the same gas phase, we can reasonably assume for Paβ the same kinematics as Hα. The mapping between wavelength and position in NIRCam grism data is only weakly wavelength and position dependent, and it is generally 10.0 Å per NIRCam F444W pixel (i.e. 10.0 Å/0.063″). Given the 50mas pixel scale of the 2D reconstructed Paβ map, a shift of one pixel results in a wavelength shift of 7.9 Å, which corresponds to 57 km s^{-1} at $\lambda \sim 4.13\,\mu$m (i.e. the observed Paβ wavelength for K20-ID7). To a first approximation, the velocity-corrected, intrinsic position along the spectral axis (i.e. $x_{\rm int}$) of a given Paβ emitting pixel at

[12] The Hα line map used in this work has been smoothed to a spatial resolution of FWHM = 0.16″ (Pulsoni et al., in prep.), whereas the nominal resolution of the ERIS AO-assisted data is FWHM = 0.105″ (Förster Schreiber et al., in prep.).

Table 3. Physical properties of the bulge, the clumps, and the whole galaxy, as resulting from our SED fitting and analysis of Paβ line emission.

	Resolved					Integrated	
	Bulge	Clump A	Clump B	Clump C	Galaxy	Galaxy$_{4.4\mu m}$	Galaxy$_{1.2mm}$
d [″]	0.25	0.8	0.5	0.3	3	3	3
$M_\star$ [10^9 M$_\odot$]	7 ± 3 $^{(\star)}$	3.5 ± 0.7	1.5 ± 0.3	0.67 ± 0.19	37 ± 10	23 ± 5	36 ± 8
t_{age} [Myr]	< 850	123 ± 75	136 ± 103	< 483	288 ± 178	< 223	413 ± 294
$A_{V,star}$ [mag]	2.83 ± 0.24	0.77 ± 0.11	1.50 ± 0.16	1.58 ± 0.21	1.01 ± 0.22	1.19 ± 0.07	1.01 ± 0.09
SFR10 [M$_\odot$ yr^{-1}]	12 ± 8 $^{(\star)}$	21 ± 6	13 ± 4	2.8 ± 1.3	109 ± 66	93 ± 20	71 ± 19
SFR100 [M$_\odot$ yr^{-1}]	82 ± 42 $^{(\star)}$	54 ± 17	18 ± 6	6 ± 3	288 ± 178	384 ± 143	146 ± 130
SFR$_{UV+IR}$ [M$_\odot$ yr^{-1}]	-	-	-	-	-	-	105 ± 17
SFR$^0_{Paβ}$ [M$_\odot$ yr^{-1}]	1.2 ± 1.0 $^{(\star)}$	21 ± 5	10 ± 2	3 ± 1	-	66 ± 22	
SFR$_{Paβ}$ [M$_\odot$ yr^{-1}]	$7.6^{+8.8}_{-6.6}$ $^{(\star)}$	24^{+6}_{-7}	11^{+2}_{-2}	$3.4^{+1.6}_{-1.0}$	-	120^{+70}_{-70}	
$A_{V,neb}$	6.43 ± 0.55	$0.4^{+0.1}_{-0.1}$	$0.4^{+0.1}_{-0.1}$	$0.4^{+0.3}_{-0.3}$	-	2.0 ± 0.6	

Notes. For the galaxy, we provide SED-based results from resolved maps (Galaxy), and integrated modeling including photometry up 4.4 μm (Galaxy$_{4.4\mu m}$) and 1.2 mm (Galaxy$_{1.2mm}$). From the top, the diameter (d) of the apertures (shown in Fig. 5) to sum or to average pixel values in resolved maps, and for the integrated analysis; the SED-based physical parameters (Sect. 4), namely, stellar mass ($M_\star$), age t_{age}) and stellar dust attenuation ($A_{V,star}$), and then SFRs averaged over the last 10 Myr and 100 Myr (SFR10 and SFR100), and derived from UV+IR luminosity (SFR$_{UV+IR}$; Paβ-based SFRs respectively inferred by assuming no dust attenuation (SFR$^0_{Paβ}$), and corrected for nebular attenuation (SFR$_{Paβ}$), through the $A_{V,neb}$ values reported in the last row (see Sect. 5.2 for details). $^{(\star)}$ $M_\star$ and SFRs of the bulge have been computed by summing over the pixels within the bulge aperture, and multiplying by two the resulting sum value (see Sect. 4.2).

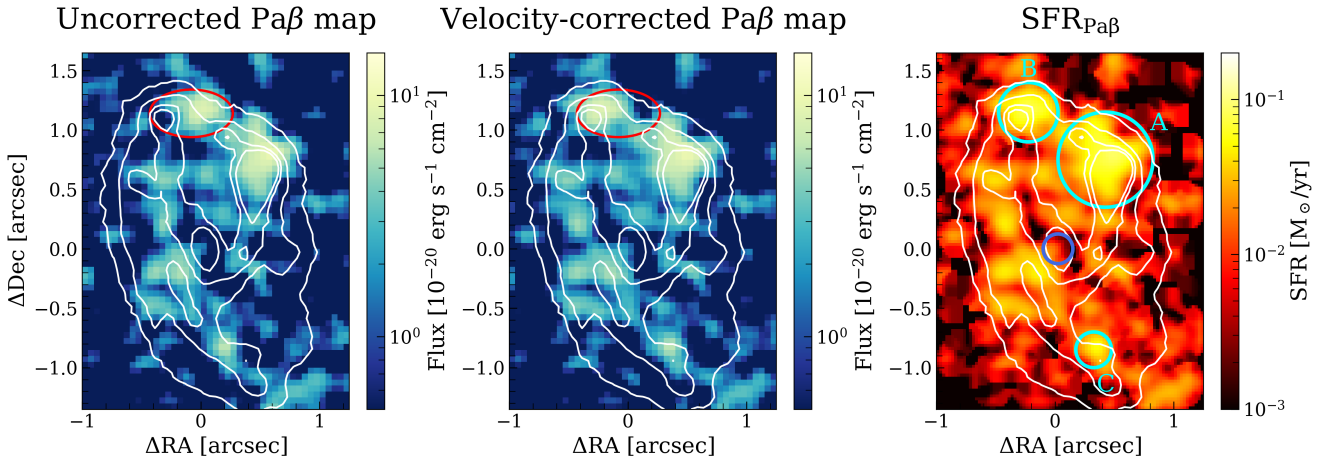

Fig. 5. 2D spatial distribution of Paβ in K20-ID7 from NIRCam grism F444W observations. *Left.* Paβ line map, as reconstructed by `grizli` (Brammer 2023), with white contours tracing F444W continuum emission. Paβ emission appears offset with respect to continuum emission, along the x-axis (i.e., grism dispersion direction), due to velocity gradients. This is particularly evident for the northernmost clump (circled in red). *Middle.* Paβ line map after correcting for the Hα velocity-field model inferred from VLT/ERIS AO data (Pulsoni et al., in prep.). Both Paβ and continuum emission now trace star-forming clumps and spiral arms well. *Right.* Paβ-traced SFR map, obtained by assuming negligible dust attenuation. Cyan circular apertures (diameters of 0.8″, 0.5″, 0.3″) and the central blue one (0.25″) are used to infer Paβ-based SFRs for the three brightest clumps and the bulge, respectively. The two Paβ maps have a 0.05″ pixel scale, while the SFR map has been rebinned to a 0.025″ pixel scale, and smoothed with a Gaussian kernel of $\sigma = 1$ pix.

a position x_{obs} in the reconstructed image can be recovered as:

$$x_{int} = x_{obs} - v(x_{int})/(57 \text{ km s}^{-1}), \quad (1)$$

where $v(x_{int})$ is the velocity value of each pixel from the rotating disk model based on the ERIS Hα data (Pulsoni et al., in in prep.).

The middle panel of Fig. 5 displays the reconstructed Paβ emission line map, after shifting each pixel along the horizontal (dispersion) axis according to Eq. 1. Although approximate, our velocity correction provides a much better spatial correspondence between Paβ and continuum emission: the Paβ emission of the northernmost clump and the galaxy spiral arms now follow well the continuum emission seen in the F444W direct image. The Paβ line distribution reveals that most of the emission arises from the clumps and spiral arms.

5.2. Star formation traced via Paβ line emission

We can now use the velocity-corrected Paβ map to spatially map recent star formation (timescale of ∼ 10 Myr), probing a more obscured regime compared to optical Balmer emission lines (e.g. Hα or Hβ). Following Reddy et al. (2023b), SFR can be inferred from the dust-corrected Paβ luminosity ($L_{Paβ}$) by means of their Eq. 2 (assuming the case $Z = 0.02$, which is the closest metallicity to our measurements), namely:

$$\text{SFR}_{Paβ}[\text{M}_\odot/\text{yr}] = 7.67 \times 10^{-41} \text{ L}_{Paβ}[\text{erg/s}]. \quad (2)$$

Since we do not have a full 2D map of nebular line attenuation and the use of the $A_{V,\rm star}$ may lead to an incorrect correction per pixel (due also to small discrepancies in the astrometric alignment), in first approximation we assume negligible attenuation at the 1.28 μm Paβ wavelength and derive a SFR map from the observed (i.e. not dust corrected) Paβ luminosity, through the pixel-by-pixel application of the equation above. The resulting Paβ-based SFR map is shown in the rightmost panel of Fig. 5, after rebinning to a 0.025″ pixelscale (to allow for direct comparison with the SFR maps shown in Fig. 4) and smoothing with a Gaussian kernel of σ=1 pixel. Table 3 reports the resulting total Paβ-based, not dust-corrected, SFRs (i.e. $\rm SFR^0_{Pa\beta}$) obtained by summing the Paβ flux within dedicated circular apertures defined for Clumps A, B and C (in cyan; diameters of 0.8″, 0.5″, 0.3″), and the bulge (in red; diameter of 0.25″). The comparison with the recent star formation (SFR10) derived from our resolved SED fitting (see Fig. 4 and SFR10 values reported in Table 3) highlights that Paβ well traces recent star formation in the clumps and in the spiral arm, where extinction is low and the star formation is indeed recent. The major difference instead comes out for the central bulge, where Paβ line emission is very weak. Consistently with the picture outlined in Sect. 4.2, this is a consequence of a low level of recent star formation and heavy extinction in the inner bulge regions, which is still important at the Paβ wavelength.

In order to place a robust lower limit on the Paβ flux in the bulge, we compute its expected value within our adopted bulge aperture, based on the SFR10 value resulting from our SED modeling and adopting two distinct values for dust attenuation, namely: 1) stellar attenuation only ($A_{V,\rm star} = 2.83 \pm 0.24$); 2) extra nebular attenuation computed as $A_{V,\rm neb} = A_{V,\rm star}\,/\,0.44 = 6.43 \pm 0.55$ (Calzetti et al. 2000). We thus obtain lower limits to the expected observed Paβ flux, which translate into lower limits to the intrinsic Paβ-based SFR, respectively, of 1.78 $\rm M_\odot\ yr^{-1}$ and 0.076 $\rm M_\odot\ yr^{-1}$, both compatible with our $\rm SFR^0_{Pa\beta}$ estimate obtained for the bulge aperture.

Finally, by fitting two Gaussian components to the 1D NIRCam WFSS spectrum (shown in Fig. 3), we infer a total Paβ flux $F_{\rm Pa\beta} = (2.2 \pm 0.7) \times 10^{-17}$ erg s^{-1} cm^{-2} for the whole galaxy, which leads to a global $\rm SFR^0_{Pa\beta} = (66 \pm 22)\ M_\odot\ yr^{-1}$. Such 1D total Pa$\beta$ flux is more reliable than the sum of the Paβ fluxes over all pixels of the (velocity-corrected) Paβ line map, which adds noise from more diffuse galaxy regions. Compared to previous published estimates (Förster Schreiber et al. 2009), our inferred total $\rm SFR^0_{Pa\beta}$ is systematically lower than the values inferred from IR luminosity and integrated HST-based SED modeling ($\rm SFR_{IR} \simeq 101\ M_\odot\ yr^{-1}$ and $\rm SFR_{SED} \simeq 110\ M_\odot\ yr^{-1}$, respectively), and closer to the total Hα-traced SFR only corrected for stellar attenuation ($\rm SFR_{H\alpha} \simeq 73\ M_\odot\ yr^{-1}$), which is known to underestimate the real nebular attenuation (e.g. Calzetti et al. 2000; Price et al. 2014; Tacchella et al. 2018). By accounting for extra attenuation of nebular line emission, Förster Schreiber et al. (2009) found $\rm SFR_{H\alpha} \simeq 190\ M_\odot\ yr^{-1}$. This furthermore indicates that Paβ still suffers from substantial attenuation in more deeply obscured regions, such as the bulge. Therefore, either neglecting extinction or not properly taking into account extra nebular attenuation at the 1.28 μm Paβ wavelength leads to underestimating the intrinsic SFR of more obscured regions, and consequently of the entire galaxy.

In Table 3, we report the local and total Paβ-based SFR ($\rm SFR_{Pa\beta}$) obtained by correcting for nebular attenuation derived from the hydrogen line ratios, namely: for Clumps A and B, and separately Clump C the values respectively inferred for Clump-N and Clump-S from MSA spectra (see Table 2); for the bulge the $A_{V,\rm neb}$ inferred from $A_{V,\rm star}$; and for the whole galaxy an average estimate based on medium- and broad-band imaging (see Appendix C). As expected, the $\rm SFR_{Pa\beta}$ of the clumps have not changed much with respect to the $\rm SFR^0_{Pa\beta}$ values, due to their low extinction; while for the bulge and the whole galaxy we now obtain consistency with the SFR10 values. In particular, we note that the total $\rm SFR_{Pa\beta}$ of the galaxy now also matches much better the global $\rm SFR_{UV+IR}$ estimate.

6. Implications on the evolution of the galaxy disk

6.1. Inside-out galaxy growth

As pointed out in Sect. 4.2, the 2D stellar age map inferred from our resolved SED fitting reveals an older stellar population in the bulge and in the nearby regions and younger ones at higher distances from the center, especially along the spiral arms and in the clumps. Despite the large non-axisymmetry, to better investigate radial trends of the various SED-inferred properties, we derive radial profiles for each physical parameter (Fig. 6), relying on the resolved SED maps of Fig. 4 and adopting six elliptical annuli, centered on the galaxy center and computed from the F444W image. Each annulus has a width of 0.25″, and is characterized by a semi-minor to semi-major axis ratio $b/a = 0.72$ (Genzel et al. 2023), and a position angle of 25° (counterclockwise from N to E; Förster Schreiber et al. 2018). As shown in Fig. 6, we compute the median value of the examined property in each elliptical annulus, and associate it with an error equal to $\pm 1\sigma$ scatter. In order to also better appreciate azimuthal scatter, for each property we also show the values of individual pixels as a function of their deprojected distance from the galaxy center, by correcting for the galaxy inclination (122° Genzel et al. 2023).

The radial profiles overall highlight the presence of a massive, highly obscured yet star-forming bulge as also seen in other cosmic noon galaxies (Arriagada-Neira et al. 2025), and they all exhibit a declining radial profile, except for the specific SFR ($\rm sSFR = SFR10\,/\,M_\star$) that features an increasing median profile, reaching the highest value in correspondence of the clumps (vertical dashed lines). The presence of clumps is one of the main elements breaking down the azimuthal symmetry of the 2D SED maps, as can also be noted from the peaks in the scatter of all properties. In particular, at the location of the clumps, we observe a decrease in stellar age, consistent with the global radial trend, which hints at an inside-out growth of the galaxy.

We further explore this inferred negative trend in stellar age by exploiting spectroscopic information. In particular, the detection of both Hα and the adjacent continuum emission in the PRISM/CLEAR data allows us to locally estimate the rest frame Hα equivalent width (EW), which is indicative of stellar population age (e.g., Levesque & Leitherer 2013). In particular, higher EWs indicate younger populations (Förster Schreiber et al. 2009, 2011; Reddy et al. 2018), since EW(Hα) depends on the ratio between the Hα line luminosity (a proxy of the current SFR) and the continuum luminosity (a proxy of the past star formation activity). Therefore, we can use the EW(Hα) as an independent age diagnostic to compare with the stellar age trend resulting from our SED-based $t_{\rm age}$ map and radial gradient. In Fig. 7, we display the EW(Hα) as a function of the sSFR for each MSA shutter (same colorcoding as in Fig. 2). In Fig. 7 we note a correlation between EW(Hα) and sSFR such that regions with larger sSFRs also have higher EWs, as previously observed in individual galaxies at $z \approx 1-3$ (Reddy et al. 2018).

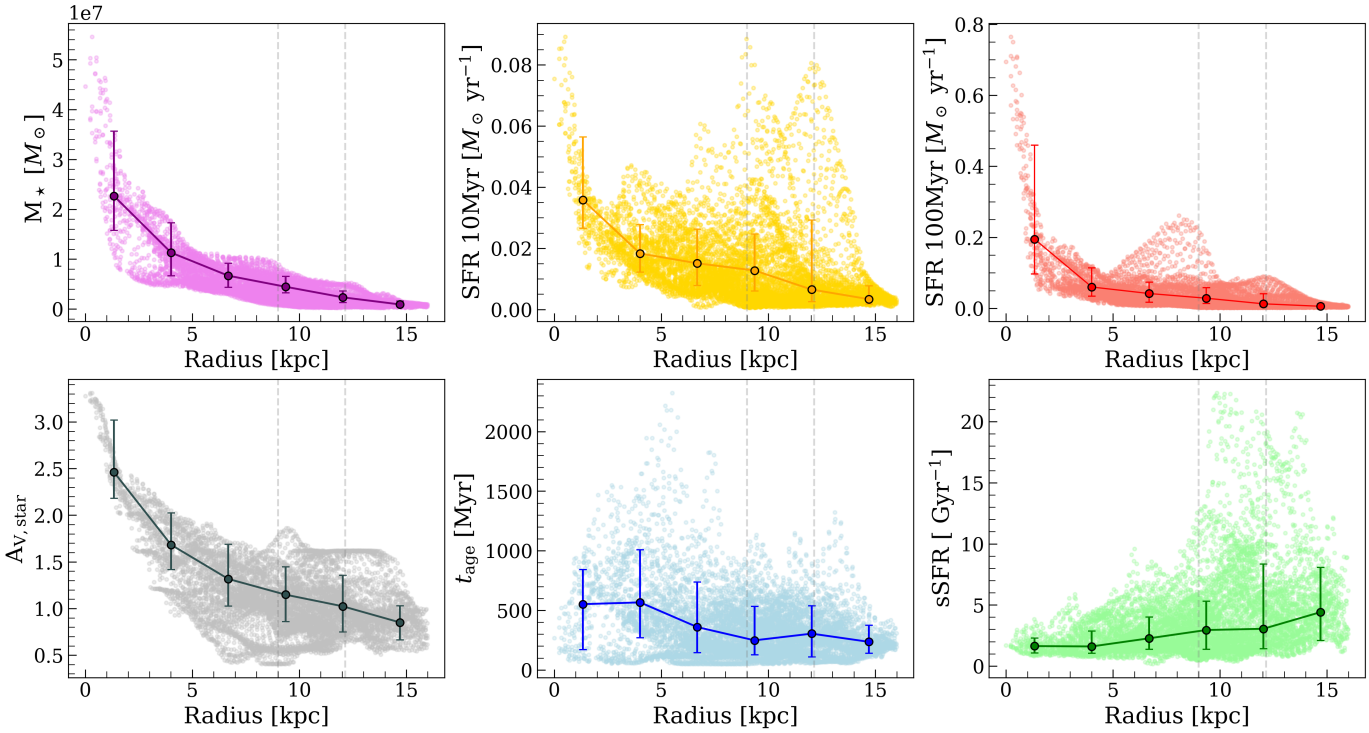

Fig. 6. Radial profiles of galaxy properties, as derived from our 2D SED-based maps. From left to right, the top panels display the radial profiles of $M_\star$, SFR10 and SFR100, while the bottom ones show $A_{V,\mathrm{star}}$, t_{age}, and specific SFR (sSFR = SFR10/M$_\star$). The big markers show the median value computed for each ring, with the errorbars showing the $\pm 1\sigma$ scatter. In the background, we plot the distribution of values of individual pixels. Vertical dashed gray lines correspond to the de-projected radii of Clump A ($\sim$ 9 kpc), and Clumps B and C($\sim$ 12 kpc).

In terms of stellar age, the Clump-N and Ext-N regions exhibit higher EW(Hα) values (EW(Hα) $\approx$ 200 Å), hinting at the presence of a younger stellar population, compared to the Inter-Arm and Ext-SW shutters (EW(Hα) $\approx$ 90 – 100 Å). The Clump-S and Arm regions display intermediate values (in spite of the large EW(Hα) uncertainty of the latter) of EW(Hα) $\approx$ 140 – 170 Å. This relative trend is in agreement with that one highlighted in our t_{age} map from resolved SED fitting (see Fig. 4). The older stellar population of the Inter-Arm region is also confirmed by the strong Balmer break in the corresponding PRISM/CLEAR spectrum (see Fig. 2). Although distinct shutters probe galaxy regions of different nature (e.g. clumps, spiral arms, inter-arm regions), if we consider the distance of each shutter from the galaxy centre, we find higher EW(Hα) values at increasing radii, in particular EW(Hα)$_{\mathrm{Inter-Arm}}$ < EW(Hα)$_{\mathrm{Arm}}$ < EW(Hα)$_{\mathrm{Clump-N}}$. This points to an "inside-out" formation scenario for K20-ID7 (Tacchella et al. 2015a; Nelson et al. 2016).

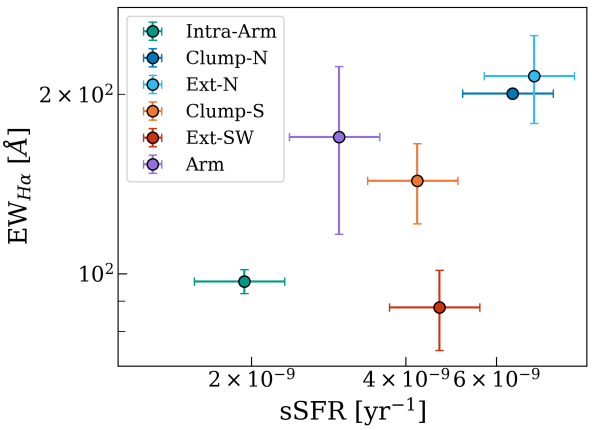

Fig. 7. Rest-frame EW(Hα) as a function of sSFR for the various galaxy regions probed by distinct MSA shutters. EW(Hα) measurements are derived from PRISM/CLEAR data, while sSFRs from our SED-based SFR10 and $M_\star$ maps. The plot highlights a correlation between the two quantities, with higher EW(Hα) values at higher sSFR, which is also indicative of younger stellar populations.

6.2. Connection with gas inflows

By exploiting high-resolution Hα SINFONI AO-assisted observations of K20-ID7, Genzel et al. (2023) found kinematic residuals indicative of rapid gas inflows at speeds of 87 km/s. More recent ERIS AO observations at higher spectral and spatial resolution have definitely confirmed the fast radial inflows and enabled a more accurate association with the spiral arms seen in the NIRCam imaging (Pulsoni et al., in prep.). The detection of such radial gas inflows, along with the results inferred in this work, supports the scenario of inflowing gas funneled from the galaxy outskirts towards the central bulge, which dilutes the metal content of the galaxy. Radial gas inflows detected along spiral arms may be fuelled by gas transport from the very outskirts of the disk, and external accretion from the circumgalactic medium (CGM), which is expected to leave imprints on the galaxy properties, if the inflowing gas is pristine or metal-poor, as we discuss in the following subsections.

6.2.1. "Diluted" gas phase metallicity

As mentioned in Sect. 3.2, the FMR predicts a metallicity $12+\log(\mathrm{O/H}) \approx 8.57$ (Curti et al. 2020b) for a galaxy with the same stellar mass and SFR as K20-ID7 (i.e. $M_\star \approx 4\times10^{10}$ $\mathrm{M}_\odot$, $\mathrm{SFR}_{\mathrm{Pa}\beta} \simeq 120\,\mathrm{M}_\odot\,\mathrm{yr}^{-1}$). At such a high SFR, the relation between metallicity and $M_\star$ is steeper, and this has been interpreted as a consequence of prominent dilution effects due to large inflows of metal-poor gas (Curti et al. 2020b).

Additional evidence supporting dilution effects due to gas inflows comes from the nitrogen abundance. The N/O we derived in Sect. 3.3 (Table 2) is interestingly 0.3 dex higher at fixed metallicity, than the best-fit relation measured for local galaxies, reported in Hayden-Pawson et al. (2022), and consistent with the large scatter observed a $z\sim2$ (Shapley et al. 2015; Hayden-Pawson et al. 2022). In contrast to oxygen and sulfur, which are α elements and are mainly created on shorter timescales in the explosion of core collapse supernovae (CCSN), nitrogen has two different creation channels (see Kobayashi & Taylor 2023, for a review): A primary channel, independent from metallicity, in which nitrogen is expelled by CCSN (Maiolino & Mannucci 2019); and a secondary channel, in which nitrogen originates from intermediate-mass, metal-rich stars reaching the asymptotic giant branch phase, which dominate the nitrogen production at high metallicity (e.g., Vincenzo et al. 2016). Given the different formation mechanism of nitrogen compared to oxygen, measuring its abundance provides insights into the star formation and chemical enrichment histories of the galaxy (Sanders et al. 2023).

With the advent of JWST, nitrogen enhancement is found to be common in very metal-poor ($Z\sim0.1\,Z_\odot$) and high-z ($z>4$) star-forming galaxies (e.g., Bunker et al. 2023; Cameron et al. 2023; Isobe et al. 2023; Topping et al. 2024), although not ubiquitous (Rogers et al. 2024). Various mechanisms were proposed to explain such a nitrogen enhancement, such as an excess of Wolf-Rayet stars (Flury et al. 2024; Welch et al. 2025), varying IMFs (Arellano-Córdova et al. 2024), or the enrichment by population III stars (Nandal et al. 2024). Considering the inflow detection in K20-ID7 (Genzel et al. 2023, Pulsoni et al. in prep.), we may here be witnessing an overall gas metallicity dilution, as traced by O/H, rather than a nitrogen enhancement (e.g., Stiavelli et al. 2025). The overabundance of N/O compared to the subsolar O/H might be a consequence of lower-metallicity gas brought in from the disk outskirts and external accretion, diluting the gas phase oxygen abundance within the disk while preserving the N/O relative abundance.

6.2.2. Low-metallicity clumps

Cosmological simulations show that gas inflows from CGM are often associated with the presence of off-center star-forming clumps, bright in Hα and poor in metals (Ceverino et al. 2016). In Sect. 3.2, we found no significant difference in the metallicity of the clumps compared to that in the other probed galaxy regions. Yet, we noted that any prominent metallicity gradients would result in being smoothed due to the spatial extent of the MSA shutters. In particular, we would expect that a large amount of metals is ejected during the explosion of massive stars in Clump-N, due to intense star formation ($\sim20\,\mathrm{M}_\odot\,\mathrm{yr}^{-1}$), in contrast to what we observe. Indeed, Clump-N is found in the same region as the strongest inflow detection (Genzel et al. 2023; Pulsoni et al., in prep.). This might suggest a possible intrinsic lower metallicity for this clump than that inferred from the Clump-N MSA data, as a consequence of accretion of pristine gas that decreases O/H abundance, while replenishing the star-forming region of gas.

An estimate of the amount of pristine gas needed to produce a given observed decrease in metallicity can be made by assuming an infall model, where the pristine inflowing gas is responsible for diluting metallicity and boosting star formation. By using Eq. 8 from Mannucci et al. (2010) and assuming a decreased metallicity of only 0.1 dex for Clump-N, we find that the accreted pristine gas in the clump should account for 20% of the mass of the gas present, to explain such a decrease in metallicity. Assuming a gas fraction of $M_{\mathrm{gas}}/M_\star = 1.8$ (Genzel et al. 2023), and considering our inferred stellar mass ($M_\star \approx 4\times10^{10}$ $\mathrm{M}_\odot$), we estimate that the pristine gas accreted on the clump is of the order of $10^9 M_\odot$. Clump-S is also located in a region where kinematic residuals point to the presence of gas inflows. With a similar reasoning as for Clump-N, it would require $\sim 10^8 M_\odot$ of accreted pristine gas to account for a 0.1 dex dilution.

6.3. Sulfur abundance at $z = 2.2$

The detection of the [SII] and [SIII] emission lines in the NIRSpec MSA spectra allowed us to locally measure the sulfur abundance of K20-ID7 (in Sect. 3.3), previously done for only a handful of galaxies at $z>1$ (e.g. Sanders et al. 2020; Rogers et al. 2024, 2025). Before the advent of JWST, detecting the [SIII] emission lines at $z\gtrsim1.5$ was indeed challenging, because they are emitted at the boundary between optical and near-IR wavelengths; therefore, they are redshifted outside the atmospheric transmission windows accessible from the ground. Sulfur is an α element (like oxygen), which is mainly produced inside the core of massive stars and then returned to the ISM on short timescales through the explosion of CCSN. Contrary to nitrogen, S/O is not supposed to depend on the metallicity of the galaxy or on the star formation history, but only on the supernova yields. Therefore, it is usually assumed to be constant throughout cosmic time, and close to the solar value ($\log(\mathrm{S/O})_\odot \sim -1.7$; Asplund et al. 2009).

In Sect. 3.3, we measure a value of $\log(\mathrm{S/O}) -2.0\pm0.2$ and -1.9 ± 0.2 for the Inter-Arm, Clump-N regions of K20-ID7. The measured value is systematically smaller than the solar value $\log(\mathrm{S/O})_\odot \sim -1.6$ (Asplund et al. 2021). or Clump-S, we still obtain a sub-solar S/O abundance but compatible with the solar one within the large uncertainties. A low S/O abundance is also observed in other $z>2$ galaxies (Rogers et al. 2024, 2025) at both low- and high-metallicities. The inferred abundance pattern might be consequence of the existence of a secondary (subdominant) production channel of sulfur through Type Ia SNe (Kobayashi et al. 2020), which leads to different oxygen and sulfur yields of oxygen and sulfur, thus altering the relative S/O abundance. The subsolar nature of these high-z sources, hence, might indicate that Type Ia SNe have not had time to explode yet. Another possible explanation for the low S/O values could be that sulfur might be captured into ice and dust grains (Hily-Blant et al. 2022; Pérez-Díaz et al. 2024). Studies of local galaxies and individual HII regions have found large scatters for S/O abundance (e.g., Díaz & Zamora 2022; Pérez-Díaz et al. 2024), with some works revealing tentative evidence of lower S/O at increasing $12+\log(\mathrm{O/H})$ (Díaz & Zamora 2022), while others do not (Izotov et al. 2006). However, a similar decreasing trend with metallicity is also observed for other α elements, which might be ascribed to the depletion of oxygen into dust grains (Izotov et al. 2006). In light of this, our measurements of abundance patterns in K20-ID7 highlight the need for caution when using nitrogen or sulfur to infer $12+\log(\mathrm{O/H})$ gas-phase metallicities (Pérez-

Díaz et al. 2024). In particular, larger samples of $z > 1$ galaxies with available S/O measurements will be needed to check on the validity at high redshift of the assumption of constant S/O abundance.

7. Conclusions

Relying on a novel set of JWST observations of K20-ID7, including both NIRSpec and NIRCam data, this work presents a comprehensive resolved study of the ISM and stellar population properties of K20-ID7, a large star-forming galaxy at $z = 2.224$ with an outstanding spiral morphology. In doing so, our analysis exploits the synergy of JWST with ground-based IFU AO observations, and introduces two main novelties in the data reduction of NIRSpec MSA spectra and in the post-processing of NIRCam WFSS data, namely: 1) the extraction of science spectra from multiple MSA shutters and and not only from the central one (as would be the case following the standard reduction procedure), thus probing in total seven distinct galaxy regions; the recovery of the intrinsic 2D spatial distribution of Paβ line emission, after correcting the Paβ line map reconstructed from NIRCam WFSS data for velocity gradients, by using the Hα velocity-field model inferred from IFU ERIS AO data at high spectral resolution ($R \sim 10500$) and comparable spatial resolution (Pulsoni et al., in prep.). Below, we summarise the main results of this work:

- By means of different emission-line diagnostics, we investigated the ISM properties in three distinct galaxy regions, namely, two clumps and an inter-arm region. Overall, we found the clumps to exhibit lower dust attenuation ($A_{V,\rm neb} \simeq 0.4$), and feature relatively low electron density ($n_{\rm e} \lesssim 300$ cm^{-3}) and ionisation parameter ($\log(U) \simeq -3.0$). As inferred from our resolved SED analysis, the clumps are found to be massive ($M_\star = 0.67 - 3.5 \times 10^9$ M$_\odot$) and have SFRs spanning about the range $3 - 20$ M$_\odot$ yr^{-1}. The inter-arm region is more dust attenuated ($A_{V,\rm neb} \simeq 1.3$), and has similar ionization conditions to the clumps. For this region, we inferred a 2σ upper limit to the electron density of $n_{\rm e} < 1900$ cm^{-3}.

- In the same regions as above, we also explore the gas phase metallicity $12 + \log(\rm O/H)$, by using strong-line diagnostics, and the chemical abundance of nitrogen and sulfur. We also obtained a metallicity measurement for a fourth region, corresponding to a spiral arm. We find no statistically significant difference in metallicity between the various regions, overall featuring $12 + \log(\rm O/H)$ values in the range $8.49 - 8.58$ and uncertainties of about $0.1 - 0.2$ dex.

- We found some evidence for metallicity patterns that are likely imprints of the known gas inflows detected in K20-ID7 (Genzel et al. 2023; Pulsoni et al., in prep.). Our inferred metallicity values are compatible with the FMR-expected metallicity (i.e. $12 + \log(\rm O/H) \approx 8.57$) for a galaxy with the same stellar mass and SFR as those we inferred for K20-ID7 (i.e. $M_\star \approx 4 \times 10^{10}$ M$_\odot$, SFR$_{\rm Pa\beta} \simeq 120$ M$_\odot$ yr^{-1}). At such high SFRs, the steepening of the $Z - M_\star$ relation points to dilution effects due to gas inflows of metal-poor gas. Similarly, such diluted metallicity could also explain the observed apparent enhancement by 0.3 dex of the log(N/O) abundance (i.e. $\simeq$ -1) in the log(N/O) – $12 + \log(\rm O/H)$ plane.

- Thanks to the detection of the [SII] and [SIII] emission lines in the NIRSpec MSA data, we measured the sulfur abundance in the Inter-Arm, and clumps regions ($12 + \log(\rm S/H)$ of $6.6^{+0.2}_{-0.2}$ for the first two, and $6.7^{+0.3}_{-0.2}$ for the third one). When combined with the $12 + \log(\rm O/H)$ values, these lead to a relative log(S/O)=-1.9, which is smaller than the expected constant (solar) value (i.e. $\log(\rm S/O) \approx -1.7$), although still compatible within the uncertainty. This might point to the existence of a secondary production channel of sulfur, via the explosion of Type I SNe on longer timescales.

- The 2D map of stellar age, derived from our resolved SED fitting, and the radial profile we extracted revealed a gradient in stellar age, with on average older stellar populations closer to the centre ($t_{\rm sge} \approx 400 - 2000$ Myr), and younger ones in more external regions (especially in the clumps, $t_{\rm sge} = 50 - 100$ Myr). Such radial decreasing trend is also supported by an inverse increasing trend in sSFR, and the Hα EWs we inferred from the NIRSpec MSA spectra for distinct galaxy regions.

- Our resolved SED analysis along with the velocity-corrected Paβ line map revealed a central moderate-massive ($M_\star = (7 \pm 3) \times 10^9$ M$_\odot$) bulge, which is highly obscured ($A_{V,\rm neb} = 6.43 \pm 0.55$), indeed still undetected in line emission at the 1.28 μm Paβ wavelength, which shows recent (~ 10 Myr) star formation (SFR10$_{\rm Bulge} = 12 \pm 8$ M$_\odot$ yr^{-1}), and even a higher activity in the past (SFR100$_{\rm Bulge} = 82 \pm 42$ M$_\odot$ yr^{-1}). Along with the relatively older stellar ages in the inner galaxy regions ($t_{\rm age} \approx 400 - 2000$ Myr), the enhanced SFR100 of the bulge supports that it assembled most of its stellar mass in the past, with still some level of active star formation.

Taking advantage of the synergy with deep ground-based AO IFU observations, this work showcases the crucial role that JWST can play in investigating key galaxy formation and evolution processes at cosmic noon. Moreover, the successful case of K20-ID7 presented in this work paves the way to similar analyses of larger samples of galaxies at cosmic noon with available spectroscopy from JWST and ground-based IFU facilities, thus enabling an accurate and complete, resolved characterization of the ISM and stellar population properties. Moreover, the discovery of the deeply obscured yet star-forming nature of the bulge of K20-ID7 underscores the importance of future high-resolution mm continuum observations with ALMA to detect obscured star formation activity in the bulge, and thus to pin down its current growth rate.

Acknowledgements. G.T., N.M.F.S, C.B., J.C. and J.M.E.S. acknowledge financial support from the European Research Council (ERC) Advanced Grant under the European Union's Horizon Europe research and innovation programme (grant agreement AdG GALPHYS, No. 101055023). HÜ and GM acknowledge funding by the European Union (ERC APEX, 101164796). Views and opinions expressed are however those of the authors only and do not necessarily reflect those of the European Union or the European Research Council Executive Agency. Neither the European Union nor the granting authority can be held responsible for them. L.S. acknowledges the financial support from the PhD grant funded on PNRR Funds Notice No. 3264 28-12-2021 PNRR M4C2 Reference IR0000034 STILES Investment 3.1 CUP C33C22000640006

References

Arellano-Córdova, K. Z., Cullen, F., Carnall, A. C., et al. 2024, arXiv e-prints, arXiv:2412.10557
Arriagada-Neira, S., Herrera-Camus, R., Villanueva, V., et al. 2025, A&A, 696, A83
Ashby, M. L. N., Willner, S. P., Fazio, G. G., et al. 2013, ApJ, 769, 80
Asplund, M., Amarsi, A. M., & Grevesse, N. 2021, A&A, 653, A141
Asplund, M., Grevesse, N., Sauval, A. J., & Scott, P. 2009, ARA&A, 47, 481

Boquien, M., Burgarella, D., Roehlly, Y., et al. 2019, A&A, 622, A103
Brammer, G. 2019, Grizli: Grism redshift and line analysis software, Astrophysics Source Code Library, record ascl:1905.001
Brammer, G. 2023, grizli
Brammer, G. B., van Dokkum, P. G., Franx, M., et al. 2012, ApJS, 200, 13
Bruzual, G. & Charlot, S. 2003, MNRAS, 344, 1000
Bunker, A. J., Cameron, A. J., Curtis-Lake, E., et al. 2024, A&A, 690, A288
Bunker, A. J., Saxena, A., Cameron, A. J., et al. 2023, A&A, 677, A88
Calzetti, D., Armus, L., Bohlin, R. C., et al. 2000, ApJ, 533, 682
Cameron, A. J., Katz, H., Rey, M. P., & Saxena, A. 2023, MNRAS, 523, 3516
Cappellari, M. 2023, MNRAS, 526, 3273
Carniani, S., Hainline, K., D'Eugenio, F., et al. 2024, Nature, 633, 318
Ceverino, D., Sánchez Almeida, J., Muñoz Tuñón, C., et al. 2016, MNRAS, 457, 2605
Chabrier, G. 2003, PASP, 115, 763
Curti, M., Maiolino, R., Cirasuolo, M., et al. 2020a, MNRAS, 492, 821
Curti, M., Mannucci, F., Cresci, G., & Maiolino, R. 2020b, MNRAS, 491, 944
Curtis-Lake, E., Carniani, S., Cameron, A., et al. 2023, Nature Astronomy, 7, 622
Dale, D. A., Helou, G., Magdis, G. E., et al. 2014, ApJ, 784, 83
Davies, R., Absil, O., Agapito, G., et al. 2023, A&A, 674, A207
Davies, R. L., Förster Schreiber, N. M., Genzel, R., et al. 2021, ApJ, 909, 78
D'Eugenio, F., Cameron, A. J., Scholtz, J., et al. 2025, ApJS, 277, 4
Díaz, A. I., Castellanos, M., Terlevich, E., & Luisa García-Vargas, M. 2000, MNRAS, 318, 462
Díaz, Á. I., Terlevich, E., Castellanos, M., & Hägele, G. F. 2007, MNRAS, 382, 251
Díaz, Á. I. & Zamora, S. 2022, MNRAS, 511, 4377
Dickinson, M., Giavalisco, M., & GOODS Team. 2003, in The Mass of Galaxies at Low and High Redshift, ed. R. Bender & A. Renzini, 324
Eisenhauer, F., Abuter, R., Bickert, K., et al. 2003, in Society of Photo-Optical Instrumentation Engineers (SPIE) Conference Series, Vol. 4841, Instrument Design and Performance for Optical/Infrared Ground-based Telescopes, ed. M. Iye & A. F. M. Moorwood, 1548–1561
Eisenstein, D. J., Johnson, B. D., Robertson, B., et al. 2023, arXiv e-prints, arXiv:2310.12340
Espejo Salcedo, J. M., Glazebrook, K., Fisher, D. B., et al. 2025a, MNRAS, 536, 1188
Espejo Salcedo, J. M., Pastras, S., Vácha, J., et al. 2025b, A&A, 700, A42
Ferreira, L., Conselice, C. J., Sazonova, E., et al. 2023, ApJ, 955, 94
Ferruit, P., Jakobsen, P., Giardino, G., et al. 2022, A&A, 661, A81
Finkelstein, S. L., Bagley, M. B., Ferguson, H. C., et al. 2023, ApJ, 946, L13
Flury, S. R., Arellano-Córdova, K. Z., Moran, E. C., & Einsig, A. 2024, arXiv e-prints, arXiv:2412.06763
Förster Schreiber, N. M., Genzel, R., Bouché, N., et al. 2009, ApJ, 706, 1364
Förster Schreiber, N. M., Renzini, A., Mancini, C., et al. 2018, ApJS, 238, 21
Förster Schreiber, N. M., Shapley, A. E., Genzel, R., et al. 2011, ApJ, 739, 45
Förster Schreiber, N. M., Übler, H., Davies, R. L., et al. 2019, ApJ, 875, 21
Förster Schreiber, N. M. & Wuyts, S. 2020, ARA&A, 58, 661
Genzel, R., Förster Schreiber, N. M., Rosario, D., et al. 2014, ApJ, 796, 7
Genzel, R., Jolly, J. B., Liu, D., et al. 2023, ApJ, 957, 48
Genzel, R., Newman, S., Jones, T., et al. 2011, ApJ, 733, 101
Giavalisco, M., Ferguson, H. C., Koekemoer, A. M., et al. 2004, ApJ, 600, L93
Giménez-Arteaga, C., Fujimoto, S., Valentino, F., et al. 2024, A&A, 686, A63
Giménez-Arteaga, C., Oesch, P. A., Brammer, G. B., et al. 2023, ApJ, 948, 126
Grogin, N. A., Kocevski, D. D., Faber, S. M., et al. 2011, ApJS, 197, 35
Hayden-Pawson, C., Curti, M., Maiolino, R., et al. 2022, MNRAS, 512, 2867
Hily-Blant, P., Pineau des Forêts, G., Faure, A., & Lique, F. 2022, A&A, 658, A168
Isobe, Y., Ouchi, M., Tominaga, N., et al. 2023, ApJ, 959, 100
Izotov, Y. I., Stasińska, G., Meynet, G., Guseva, N. G., & Thuan, T. X. 2006, A&A, 448, 955
Jakobsen, P., Ferruit, P., Alves de Oliveira, C., et al. 2022, A&A, 661, A80
Ju, M., Wang, X., Jones, T., et al. 2025, ApJ, 978, L39
Kalita, B. S., Suzuki, T. L., Kashino, D., et al. 2025, MNRAS, 536, 3090
Kashino, D., Lilly, S. J., Matthee, J., et al. 2023, ApJ, 950, 66
Kennicutt, R. C. & Evans, N. J. 2012, ARA&A, 50, 531
Kennicutt, Jr., R. C. 1998, ARA&A, 36, 189
Kobayashi, C., Karakas, A. I., & Lugaro, M. 2020, ApJ, 900, 179
Kobayashi, C. & Taylor, P. 2023, arXiv e-prints, arXiv:2302.07255
Koekemoer, A. M., Faber, S. M., Ferguson, H. C., et al. 2011, ApJS, 197, 36
Lang, P., Wuyts, S., Somerville, R. S., et al. 2014, ApJ, 788, 11
Levesque, E. M. & Leitherer, C. 2013, ApJ, 779, 170
Li, J., Da Cunha, E., González-López, J., et al. 2024, ApJ, 976, 70
Lines, N. E. P., Bowler, R. A. A., Adams, N. J., et al. 2025, MNRAS, 539, 2685
Lorenz, B., Suess, K. A., Kriek, M., et al. 2025, arXiv e-prints, arXiv:2505.10632
Lutz, D., Poglitsch, A., Altieri, B., et al. 2011, A&A, 532, A90
Madau, P. & Dickinson, M. 2014, ARA&A, 52, 415
Maiolino, R. & Mannucci, F. 2019, A&A Rev., 27, 3
Mannucci, F., Cresci, G., Maiolino, R., Marconi, A., & Gnerucci, A. 2010, MNRAS, 408, 2115
Maraston, C., Pforr, J., Renzini, A., et al. 2010, MNRAS, 407, 830
Markov, V., Gallerani, S., Ferrara, A., et al. 2025, Nature Astronomy, 9, 458
Masters, D., Faisst, A., & Capak, P. 2016, ApJ, 828, 18
Matharu, J., Papovich, C., Simons, R. C., et al. 2022, ApJ, 937, 16
Naidu, R. P., Oesch, P. A., Brammer, G., et al. 2025, arXiv e-prints, arXiv:2505.11263
Nandal, D., Regan, J. A., Woods, T. E., et al. 2024, A&A, 683, A156
Nelson, E., Brammer, G., Giménez-Arteaga, C., et al. 2024, ApJ, 976, L27
Nelson, E. J., van Dokkum, P. G., Förster Schreiber, N. M., et al. 2016, ApJ, 828, 27
Nestor Shachar, A., Sternberg, A., Genzel, R., et al. 2025, arXiv e-prints, arXiv:2503.00839
Neufeld, C., van Dokkum, P., Asali, Y., et al. 2024, ApJ, 972, 156
Oesch, P. A., Brammer, G., Naidu, R. P., et al. 2023, MNRAS, 525, 2864
Osterbrock, D. E. & Ferland, G. J. 2006, Astrophysics of gaseous nebulae and active galactic nuclei
Park, M., Belli, S., Conroy, C., et al. 2024, ApJ, 976, 72
Pérez-Díaz, B., Pérez-Montero, E., Fernández-Ontiveros, J. A., et al. 2024, A&A, 685, A168
Pilyugin, L. S., Vílchez, J. M., Mattsson, L., & Thuan, T. X. 2012, MNRAS, 421, 1624
Planck Collaboration, Ade, P. A. R., Aghanim, N., et al. 2016, A&A, 594, A13
Price, S. H., Kriek, M., Brammer, G. B., et al. 2014, ApJ, 788, 86
Reddy, N. A., Shapley, A. E., Sanders, R. L., et al. 2018, ApJ, 869, 92
Reddy, N. A., Shapley, A. E., Sanders, R. L., et al. 2025, arXiv e-prints, arXiv:2506.17396
Reddy, N. A., Topping, M. W., Sanders, R. L., Shapley, A. E., & Brammer, G. 2023a, ApJ, 952, 167
Reddy, N. A., Topping, M. W., Sanders, R. L., Shapley, A. E., & Brammer, G. 2023b, ApJ, 948, 83
Rieke, M. J., Kelly, D. M., Misselt, K., et al. 2023, PASP, 135, 028001
Rogers, N. S. J., Strom, A. L., Rudie, G. C., et al. 2024, ApJ, 964, L12
Rogers, N. S. J., Strom, A. L., Rudie, G. C., et al. 2025, arXiv e-prints, arXiv:2509.18257
Sanders, R. L., Jones, T., Shapley, A. E., et al. 2020, ApJ, 888, L11
Sanders, R. L., Shapley, A. E., Clarke, L., et al. 2023, ApJ, 943, 75
Sanders, R. L., Shapley, A. E., Kriek, M., et al. 2016, ApJ, 816, 23
Sanders, R. L., Shapley, A. E., Topping, M. W., et al. 2025, arXiv e-prints, arXiv:2508.10099
Scholtz, J., Carniani, S., Parlanti, E., et al. 2025, arXiv e-prints, arXiv:2510.01034
Shapley, A. E., Reddy, N. A., Kriek, M., et al. 2015, ApJ, 801, 88
Shen, L., Papovich, C., Matharu, J., et al. 2024, ApJ, 963, L49
Skelton, R. E., Whitaker, K. E., Momcheva, I. G., et al. 2014, ApJS, 214, 24
Slob, M., Kriek, M., de Graaff, A., et al. 2025, arXiv e-prints, arXiv:2506.04310
Sorba, R. & Sawicki, M. 2018, MNRAS, 476, 1532
Speagle, J. S., Steinhardt, C. L., Capak, P. L., & Silverman, J. D. 2014, ApJS, 214, 15
Steidel, C. C., Strom, A. L., Pettini, M., et al. 2016, ApJ, 826, 159
Stiavelli, M., Morishita, T., Chiaberge, M., et al. 2025, ApJ, 981, 136
Strom, A. L., Steidel, C. C., Rudie, G. C., Trainor, R. F., & Pettini, M. 2018, ApJ, 868, 117
Tacchella, S., Carollo, C. M., Förster Schreiber, N. M., et al. 2018, ApJ, 859, 56
Tacchella, S., Carollo, C. M., Renzini, A., et al. 2015a, Science, 348, 314
Tacchella, S., Lang, P., Carollo, C. M., et al. 2015b, ApJ, 802, 101
Tacconi, L. J., Genzel, R., & Sternberg, A. 2020, ARA&A, 58, 157
Toomre, A. 1964, ApJ, 139, 1217
Topping, M. W., Sanders, R. L., Shapley, A. E., et al. 2025, arXiv e-prints, arXiv:2502.08712
Topping, M. W., Stark, D. P., Senchyna, P., et al. 2024, MNRAS, 529, 3301
Vazdekis, A., Sánchez-Blázquez, P., Falcón-Barroso, J., et al. 2010, MNRAS, 404, 1639
Vincenzo, F., Belfiore, F., Maiolino, R., Matteucci, F., & Ventura, P. 2016, MNRAS, 458, 3466
Walter, F., Carilli, C., Neeleman, M., et al. 2020, ApJ, 902, 111
Welch, B., Rivera-Thorsen, T. E., Rigby, J. R., et al. 2025, ApJ, 980, 33
Whitaker, K. E., Franx, M., Leja, J., et al. 2014, ApJ, 795, 104
Wuyts, S., Förster Schreiber, N. M., Genzel, R., et al. 2012, ApJ, 753, 114
Wuyts, S., Förster Schreiber, N. M., Nelson, E. J., et al. 2013, ApJ, 779, 135

[1] Max-Planck-Institut für extraterrestrische Physik (MPE), Gießenbachstraße 1, 85748 Garching, Germany
[2] Scuola Normale Superiore, Piazza dei Cavalieri 7, I-56126 Pisa, Italy
[3] Department of Physics and Astronomy "Augusto Righi", University of Bologna, Via Piero Gobetti 93/2, I-40129 Bologna, Italy
[4] INAF – Astrophysics and Space Science Observatory of Bologna, Via Piero Gobetti 93/3, I-40129 Bologna, Italy
[5] Max-Planck-Institut für Astrophysik (MPA), Karl-SchwarzschildStr. 1, D-85748 Garching, Germany
[6] Department of Astronomy, University of Geneva, Chemin Pegasi 51, CH1290 Versoix, Switzerland
[7] Cosmic Dawn Center (DAWN), Niels Bohr Institute, University of Copenhagen, Jagtvej 128, DK-2200 København N, Denmark
[8] European Southern Observatory, Karl-Schwarzschild-Str. 2, 85748, Garching bei München, Germany
[9] INAF - Osservatorio Astrofisico di Arcetri, Largo E. Fermi 5, I-50125, Florence, Italy
[10] Department of Physics, Technical University of Munich, 85748 Garching, Germany
[11] Departments of Physics and Astronomy, University of California, Berkeley, CA 94720, USA
[12] Departamento de Astronomía, Universidad de Concepción, Barrio Universitario, Concepción, Chile
[13] DTU-Space, Technical University of Denmark, Elektrovej 327, DK2800 Kgs. Lyngby, Denmark
[14] Purple Mountain Observatory, Chinese Academy of Sciences, 10 Yuanhua Road, Nanjing 210023, China
[15] School of Physics and Astronomy, Tel Aviv University, Tel Aviv 69978, Israel
[16] Space Telescope Science Institute (STScI), 3700 San Martin Drive, Baltimore, MD 21218, USA
[17] Osservatorio Astronomico di Padova, Vicolo dell'Osservatorio 5, Padova, I-35122, Italy
[18] University of Trento, Via Sommarive 14, Trento, I-38123, Italy
[19] Dipartimento di Fisica e Astronomia, Università di Firenze, Via G. Sansone 1, I-50019, Sesto F.no (Firenze), Italy
[20] Department of Physics, University of Bath, Claverton Down, Bath, BA2 7AY, UK
e-mail: eleonora.parlanti@sns.it, gtozzi@mpe.mpg.de

Appendix A: Spectral fitting of NIRSpec MSA data

In this appendix, we provide details on the spectral fitting of the NIRSpec MSA spectra of K20-ID7, at low spectral resolution and separately for the medium- and high-resolution gratings. In the PRISM/CLEAR spectra, stellar continuum is well detected and close emission lines are blended together (e.g. Hβ + [OIII], Hα + [NII], [SII] line doublet). On the contrary, in medium- and high-resolution data continuum emission is faint and the emission lines are separately detected, although spectrally resolved only with the high-resolution ($R \sim 2700$) grating G395H/F290LP. The best-fit results obtained for the emission lines detected at $S/N > 3$ are listed in Table A.1, separately for data at different spectral resolution. Lines simultaneously observed with different gratings have mostly fluxes consistent within the errors, or they differ by less than $\sim 20\%$, compatible with the known (undesired) differences in the flux calibration at different resolution (e.g., D'Eugenio et al. 2025). For this reason, we caution on the absolute value of the inferred line fluxes, which should preferably be used for a relative comparison between different galaxy regions.

Appendix A.1: Low-resolution spectra

As shown in Fig. 2, the PRISM/CLEAR spectra of K20-ID7 exhibit a prominent continuum emission (especially Clump-N, Clump-S, and Inter-Arm), in addition to numerous (spectrally unresolved) emission lines. We fit the full (continuum plus emission lines) spectra by means of the Penalized PiXel-Fitting code (`pPXF`; Cappellari 2023), which models continuum emission through a linear combination of simple stellar population (SSP) models, and emission lines by means of Gaussian components. We use stellar templates from the MILES SSP library (Vazdekis et al. 2010), and constrain all emission lines to have the same kinematics (i.e., velocity and velocity dispersion). The line ratios of [OIII]λ5007/[OIII]λ4959 and [NII]λ6584/[NII]λ6548 are also fixed to 2.98 and 2.94, respectively, according to atomic physics prescriptions (see Osterbrock & Ferland 2006). The best-fit continuum emission is then used as a continuum input for the subsequent fitting of the emission lines.

After this first fitting with `pPXF`, we subtract the best-fit continuum model from the data and perform a refined modeling of the emission lines only, with a custom `python` script to properly account for the poor and variable spectral resolution of the PRISM/CLEAR data (varying from R$\sim$30 at $\sim$1.1μm to R$\sim$400 at the reddest wavelength, see Jakobsen et al. 2022), and accurately estimate the flux of the emission lines and the relative error. As done in the previous fitting with `pPXF`, we constrain all lines to the same velocity and fit [OIII] and [NII] line doublets with a fixed line ratio. To account for the varying spectral resolution of the PRISM data, we tie the velocity dispersion only between lines that are close in wavelength (e.g., [OIII] and Hβ). Moreover, due to the poor spectral resolution of PRISM data (i.e. $R = 100$), [NII] and Hα emission lines appear blended together. Since they are separately resolved in the medium-resolution spectra, and we are interested in estimating the Hα flux to compute the Hα equivalent width (EW(Hα), see Sect. 6.1), we fix the [NII]λ6584/Hα line ratio to the one measured in the corresponding G235M/F170LP data from the same shutter (if detected), otherwise to the one measured in the G235M/F170LP data from the adjacent shutter. The [OII]$\lambda\lambda$3727,29 and the [SII]$\lambda\lambda$6716, 31 line doublets are also unresolved in the PRISM spectra. For simplicity, we fit each doublet with a single Gaussian component.

Following all the prescriptions above, we perform the spectral fitting using the `python` package `LMFIT`, which delivers the best-fit values of the amplitude, line width, and velocity of each emission line, which minimize the χ^2. In Fig. A.1, we show all PRISM spectra available along with their best-fit model, given by the sum of the continuum model obtained with `pPXF` and Gaussian emission lines from `LMFIT`. Stellar continuum and emission lines are detected in all spectra but the External-SE shutter (in pink in Fig. 2), where only continuum emission is detected. To accurately estimate line fluxes and errors, we follow a Monte Carlo approach and, therefore, perturb the observed spectrum with its associated noise spectrum (from the 'error' extension of the data), and repeat the emission-line fitting 200 times, with the line setting described above. In Table A.1, we report the median flux value and the 1σ uncertainty obtained via a Monte Carlo technique for all emission lines detected with a $S/N > 3$.

Appendix A.2: Medium- and high-resolution spectra

Following slightly different prescriptions, we fit the medium- and high-resolution spectra (each grating separately). Unlike in the PRISM data, continuum emission is only barely detected in $R = 1000$ and $R = 2700$ data, and does not show significant stellar features to require an accurate modeling with SSPs. Therefore, there is no need to use `pPXF`, and directly perform the emission line modeling with `LMFIT`, including a second-order polynomial to reproduce the faint detected continuum emission. Since the spectral resolution has a smaller variation with wavelength in the medium- and high-resolution grating (see Jakobsen et al. 2022) (also because each grating covers a total smaller wavelength range), we constrain all lines within the same grating to have the same velocity and velocity dispersion. We still fix the flux ratios of the [NII]and [OIII]line doublets to the theoretical ratios, whereas we fit each line of the [SII]$\lambda\lambda$6716, 31 doublet with two separate Gaussian components, since the two lines are here resolved. The [OII]$\lambda\lambda$3727,29 line doublet, unfortunately, falls into the detector gap of the G140M/F070LP data, hence it is not detected. As for the PRISM data, in Table A.1 we report the median flux values and the 1σ errors for each emission line with a $S/N > 3$, as resulting from a Monte Carlo simulation.

Given the range of velocity dispersion measured for K20-ID7 ranging from 20 to 140 km s^{-1} (see Förster Schreiber et al. 2018, Pulsoni et al. in prep), the lines result in being spectrally unresolved in the medium-resolution data at $R \sim 1000$ (corresponding to a FWHM $\sim$ 300 km/s). Emission lines are instead spectrally resolved at $R \sim 2700$. For them, we also report in Table A.1 the intrinsic velocity dispersion, obtained from the observed one after correcting for the instrument spectral resolution.

Appendix B: Resolved SED best models

Figure B.1 shows the observed SEDs and the best-fit models, resulting from our resolved SED fitting with `CIGALE` (performed in Sect. 4.1), for four individual pixels representative of distinct galaxy regions (top and middle panels), namely: Clump-N (or Clump A), the bulge, the spiral arm and the inter-arm region south-east and north of the bulge, respectively. Bottom panels show the best fits of the integrated SED modeling (obtained in Sect. 4.3), including photometry up to NIRCam F444W (left) and ALMA Band 6 1.2 mm (right).

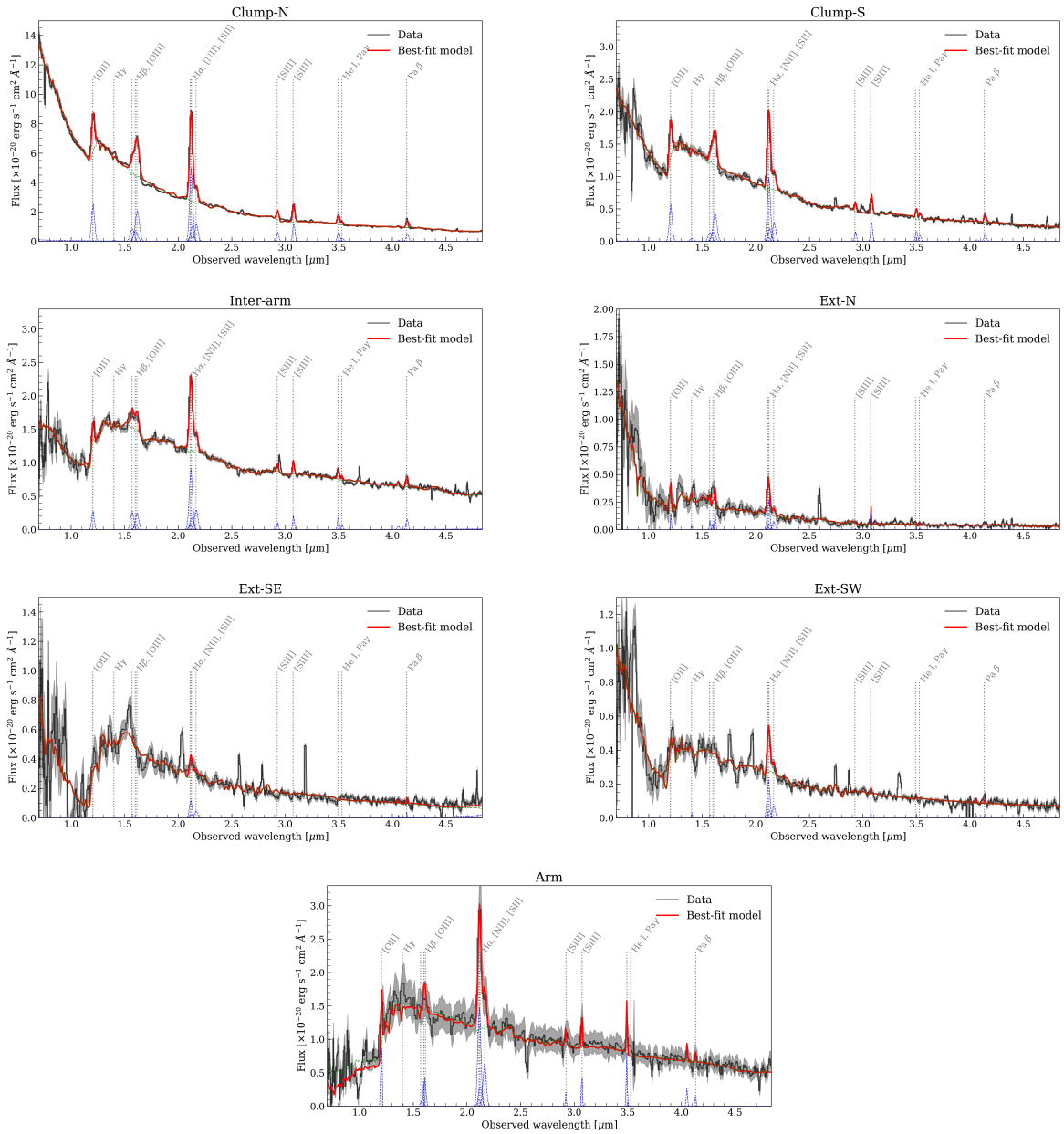

Fig. A.1. NIRSpec MSA PRISM/CLEAR spectra ($R = 100$) of K20-ID7, from all six shutters. Data are shown in black, with the best-fit model overplotted in red. All spectra exhibit both stellar continuum and emission lines, except for the External-SE spectrum, where we only detect continuum emission.

Appendix C: Nebular A_V from NIRCam imaging

In addition to the stellar $A_{V,\mathrm{star}}$ map inferred from SED fitting in Sect. 4, we derive an independent map of nebular $A_{V,\mathrm{neb}}$ from Paβ/Hα ratios, as inferred by combining available medium-band NIRCam imaging containing Hα and Paβ (i.e. F210M and F410M, respectively), and broad-band NIRCam filters (see also Lorenz et al. 2025). We first fit a 3rd-degree polynomial to the broad-band photometry of each pixel, only considering filters at longer wavelengths than the Balmer break (i.e. F150W, F200W, F277W, F356W, F444W), in order to derive continuum emission. In the polynomial fitting, we associate a small uncertainty (i.e., 1%) to the flux of filters with no significant line emission, whereas larger uncertainties of 10% and 5% to the F200W and F444W fluxes, respectively, to account for Hα and Paβ emission-line contribution to the total broadband emission. Then, we convolve the continuum best-fit model of each pixel with the F210M and F410M filter transmission, respectively, and integrate the convolved continuum model over the wavelength range of the corresponding filter, thus separately obtaining the contribution of continuum emission to the F210M and F410M bands. By removing the inferred continuum level from the total observed F210M and F410M flux in each pixel, we end up with residual line emission, including also contributions from emission lines other than Hα and Paβ. In particular, line emission of K20-ID7 in the F210M and F410M filters is mostly due to Hα +[NII] and Paβ +[FeII], respectively. Therefore, to obtain an estimate of the Hα and Paβ fluxes only, we correct the resulting total line fluxes by adopting Hα/[NII] and Paβ/[FeII] line ratios, as measured from the MSA spectra. In particular, for the northern clumps (i.e. Clump-N and the smaller northernmost clump) we adopt the flux measurements obtained for Clump-N (Hα/[NII] = 5.1 and

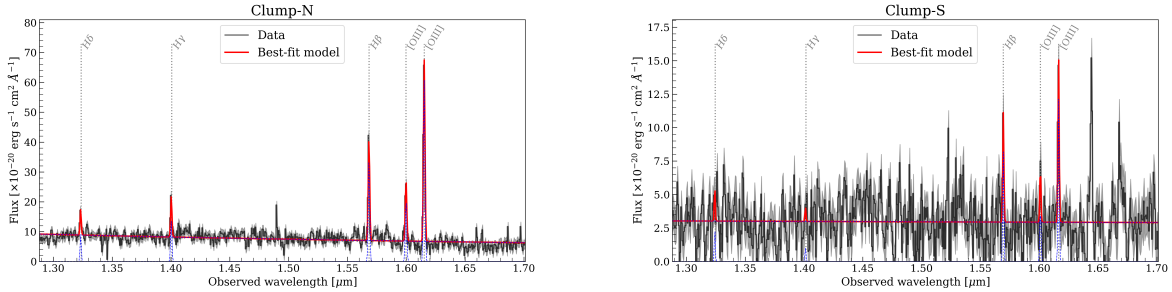

Fig. A.2. NIRSpec MSA medium-resolution spectra ($R = 1000$) of K20-ID7, obtained with the G140M/F070LP grating, for the shutters where we detect emission lines at S/N>3. Data are shown in black, with the best-fit model overplotted in red.

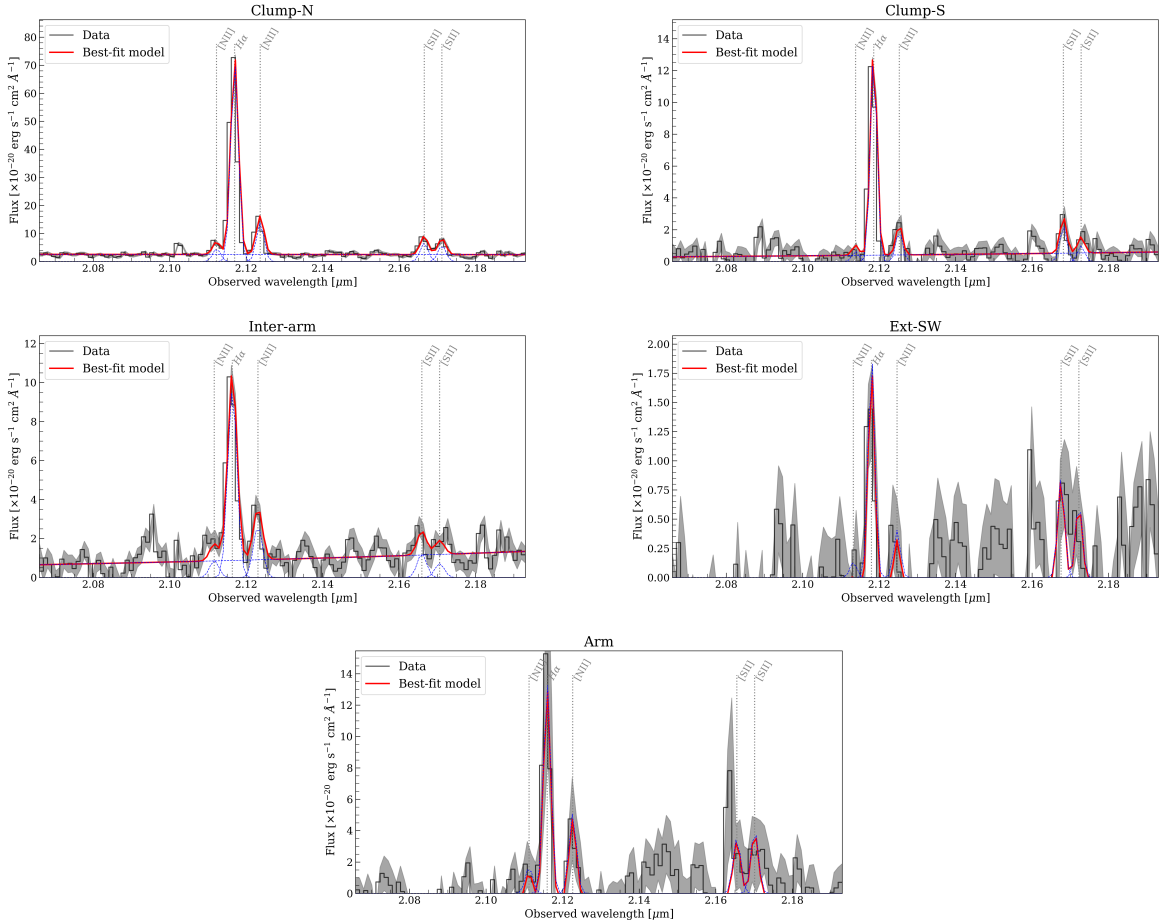

Fig. A.3. NIRSpec MSA medium-resolution spectra ($R = 1000$) of K20-ID7, obtained with the G235M/F170LP grating around the Hα, [NII] complex for the shutters where we detect emission lines at S/N>3. Data are shown in black, with the best-fit model overplotted in red.

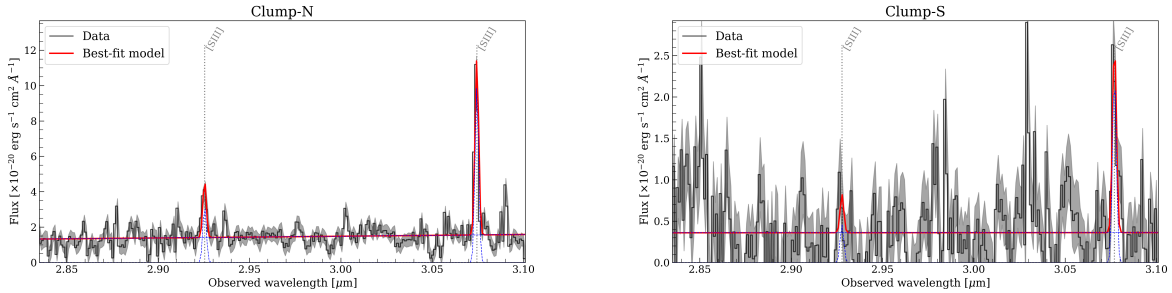

Fig. A.4. NIRSpec MSA medium-resolution spectra ($R = 1000$) of K20-ID7, obtained with the G235M/F170LP grating around the [SIII] emission lines for the shutters where we detect emission lines at S/N>3. Data are shown in black, with the best-fit model overplotted in red.

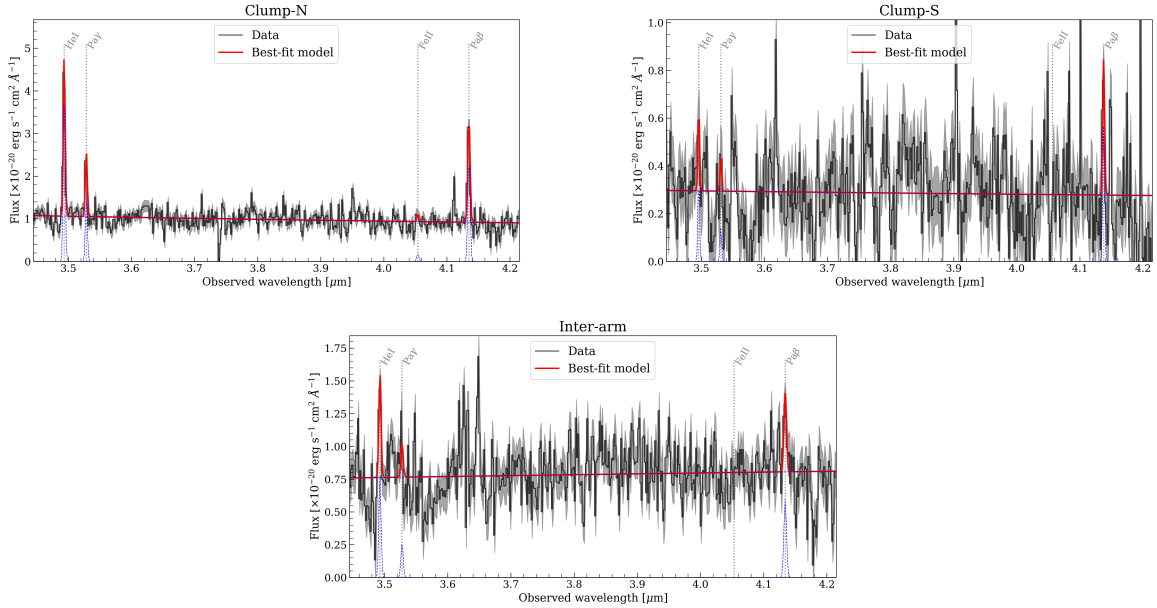

Fig. A.5. NIRSpec MSA high-resolution spectra ($R = 1000$) of K20-ID7, obtained with the G395M/F290LP, for the shutters where we detect emission lines at S/N>3. Data are shown in black, with the best-fit model overplotted in red.

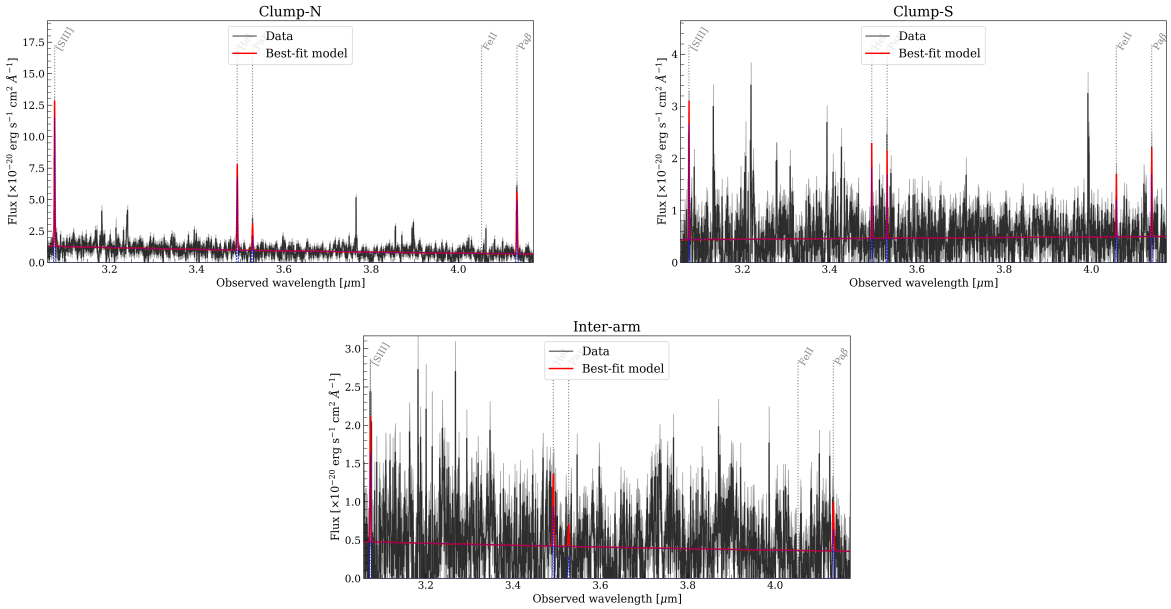

Fig. A.6. NIRSpec MSA high-resolution spectra ($R = 2700$) of K20-ID7, obtained with the G395H/F290LP, for the shutters where we detect emission lines at S/N>3. Data are shown in black, with the best-fit model overplotted in red.

Paβ/[FeII] = 14); while for all the rest of the galaxy (i.e. spiral arms, inter-arm regions, and bulge), we rely on the line ratios inferred for the Inter-Arm and/or Arm region, when available (i.e. Paβ/[FeII] = 8.4 from Inter-Arm spectra; Hα/[NII] = 3.0, computed as average between line ratios measured from the Inter-Arm and Arm regions).

In Fig. C.1, we show the resulting maps of observed (i.e. not dust-corrected) Hα and Paβ flux, along with the nebular $A_{V,\mathrm{neb}}$ map, as obtained from pixel-per-pixel Paβ/Hα line ratios, according to a Calzetti et al. (2000) dust attenuation law ($R_V = 4.05$). Unfortunately, due to faintness of the Paβ line emission compared to the continuum, this approximate procedure allows us to recover only Paβ line flux in part of the most actively star-forming regions (i.e., clumps and spiral arms). Apparently Paβ is also detected in the bulge, as opposed to the NIRCam WFSS Paβ map (shown in Fig. 5). For this reason, we caution on the reliability of the Paβ detection in the inner central regions. The right-hand panel of Fig. C.1 displays the resulting $A_{V,\mathrm{neb}}$ map inferred from Paβ/Hα line ratios, after masking pixels with (non-physical) negative $A_{V,\mathrm{neb}}$ values. Given the sparse nature of the resulting $A_{V,\mathrm{neb}}$ map, we estimate the average $A_{V,\mathrm{neb}}$ value, after masking pixels within our 0.25″-diameter bulge aperture (being them subject to the large uncertain on the Paβ line flux), and adopt this value as indicative of the global dust attenuation of the galaxy, assuming an uncertainty of 30% (i.e. $A_{V,\mathrm{neb}} = 2.0 \pm 0.6$).

Table A.1. Best-fit results for emission lines detected at S/N > 3 in the NIRSpec MSA spectra of K20-ID7 at different spectral resolution.

Line	PRISM/CLEAR						G140M/F070LP, G235M/F170LP, G395M/F290LP (G395H/F290LP)				
	Arm	Inter-Arm	Clump-N	Ext-N	Clump-S	Ext-SW	Arm	Inter-Arm	Clump-N	Clump-S	Ext-SW
[OII]$\lambda\lambda$3727,29	-	85 ± 33 (*)	917 ± 43 (*)	-	184 ± 34 (*)	-	-	-	-	-	-
Hδ	-	-	-	-	-	-	-	-	111 ± 14	-	-
Hγ	-	-	20 ± 1	-	-	-	-	-	191 ± 16	-	-
Hβ	-	-	380 ± 31	-	-	-	-	-	525 ± 18	102 ± 15	-
[OIII]λ5007	-	-	997 ± 35	-	192 ± 24	-	-	112 ± 23	972 ± 18	155 ± 17	-
Hα	606 ± 190	350 ± 16	1782 ± 22	83 ± 14	355 ± 13	65 ± 10	332 ± 45	293 ± 13	1792 ± 12	281 ± 10	41 ± 10
[NII]	-	70 ± 4	357 ± 4	-	71 ± 3	-	136 ± 40	82 ± 10	351 ± 9	40 ± 9	-
[SII]λ6717	-	122 ± 19 (*)	424 ± 20 (*)	-	108 ± 15 (*)	-	-	37 ± 11	171 ± 9	47 ± 10	-
[SII]λ6731	-	-	-	-	-	-	-	24 ± 11	148 ± 10	20 ± 9	-
[SIII]λ9069	-	-	153 ± 9	-	30 ± 7	-	-	-	76 ± 8	-	-
[SIII]λ9533	-	34 ± 12	325 ± 10	-	61 ± 9	-	-	-	249 ± 8	65 ± 15	-
	-	-	-	-	-	-	-	(39 ± 5)	(218 ± 6)	(33 ± 4)	-
HeIλ1.083	-	41 ± 10	175 ± 7	-	40 ± 6	-	-	33 ± 6	146 ± 5	11 ± 4	-
	-	-	-	-	-	-	-	(24 ± 5)	(144 ± 6)	(24 ± 6)	-
Paγ	-	-	60 ± 6	-	20 ± 4	-	-	-	59 ± 4	-	-
	-	-	-	-	-	-	-	-	(46 ± 5)	(22 ± 3)	-
Paβ	-	35 ± 7	151 ± 7	-	29 ± 5	-	-	30 ± 6	112 ± 4	22 ± 5	-
	-	-	-	-	-	-	-	(20 ± 5)	(127 ± 5)	(26 ± 4)	-
σ_{gas}	-	-	-	-	-	-	-	(79 ± 10)	(55 ± 2)	(44 ± 3)	-

Notes. All fluxes are in units of 10^{-20} erg s^{-1} cm^{-2}. For the reddest G395M and G395H gratings, we provide line fluxes measured at both medium and high spectral resolution (the latter in brackets). The last row reports the intrinsic velocity dispersion σ_{gas} (i.e. corrected for instrumental broadening) in units of km s^{-1}, as measured in high-resolution G395H data. (*) Total fluxes computed as the sum of the flux of the two [OII]$\lambda\lambda$3727,29 and [SII]$\lambda\lambda$6716, 31 doublet components, which are unresolved in PRISM/CLEAR spectra ($R = 100$).

Appendix D: Validating resolved SED fitting results

To check on the reliability of the results of our spatially resolved SED fitting, we recover the expected observed Hα flux by combining the SFR10 and $A_{V,star}$ maps. As we discussed in Sects. 5-6, nebular line emission is expected to be subject to extra attenuation compared to the stellar populations in regions of intense star formation (e.g. Calzetti et al. 2000; Price et al. 2014; Tacchella et al. 2018). Therefore, we here use in first approximation the $A_{V,star}$ map – the only full A_V map we could recover –, being aware of the fact that it might locally underestimate the real attenuation of Hα line emission. In particular, we first convert the SFR10 into Hα intrinsic luminosity according to the Kennicutt & Evans (2012) relation, which is in turn converted into the observed Hα flux by (de-)correcting for dust attenuation (Calzetti et al. 2000) law, using the $A_{V,star}$ values previously inferred for each single pixel. In Fig. D.1 we show the comparison of our recovered observed Hα flux (left-hand panel) with the real observed one from ERIS observations (right-hand panel, same colorscale; Forster Schreiber et al., in prep.; Pulsoni et al., in prep.). The striking similarity between the two Hα maps points to the reliability of our SFR10 map, although some degeneracy might still be present between SFR10 and $A_{V,star}$ values for a given observed Hα flux. By summing over all pixels, we obtain a total recovered Hα flux of 2.0×10^{-16} erg s^{-1} cm^{-2}, which is consistent with the total Hα flux measured from ERIS and SINFONI data (Förster Schreiber et al. 2009). We note that, although in principle it is possible to insert as input in `CIGALE` also emission-line fluxes, we do not do it because of the difficulties in correctly aligning (on a pixel level of 0.025″) the NIRCam, ACS, and ERIS data. This test highlights that we are able not only to correctly recover the total Hα flux, but also its spatial distribution, showing the reliability of our spatially resolved SED analysis.

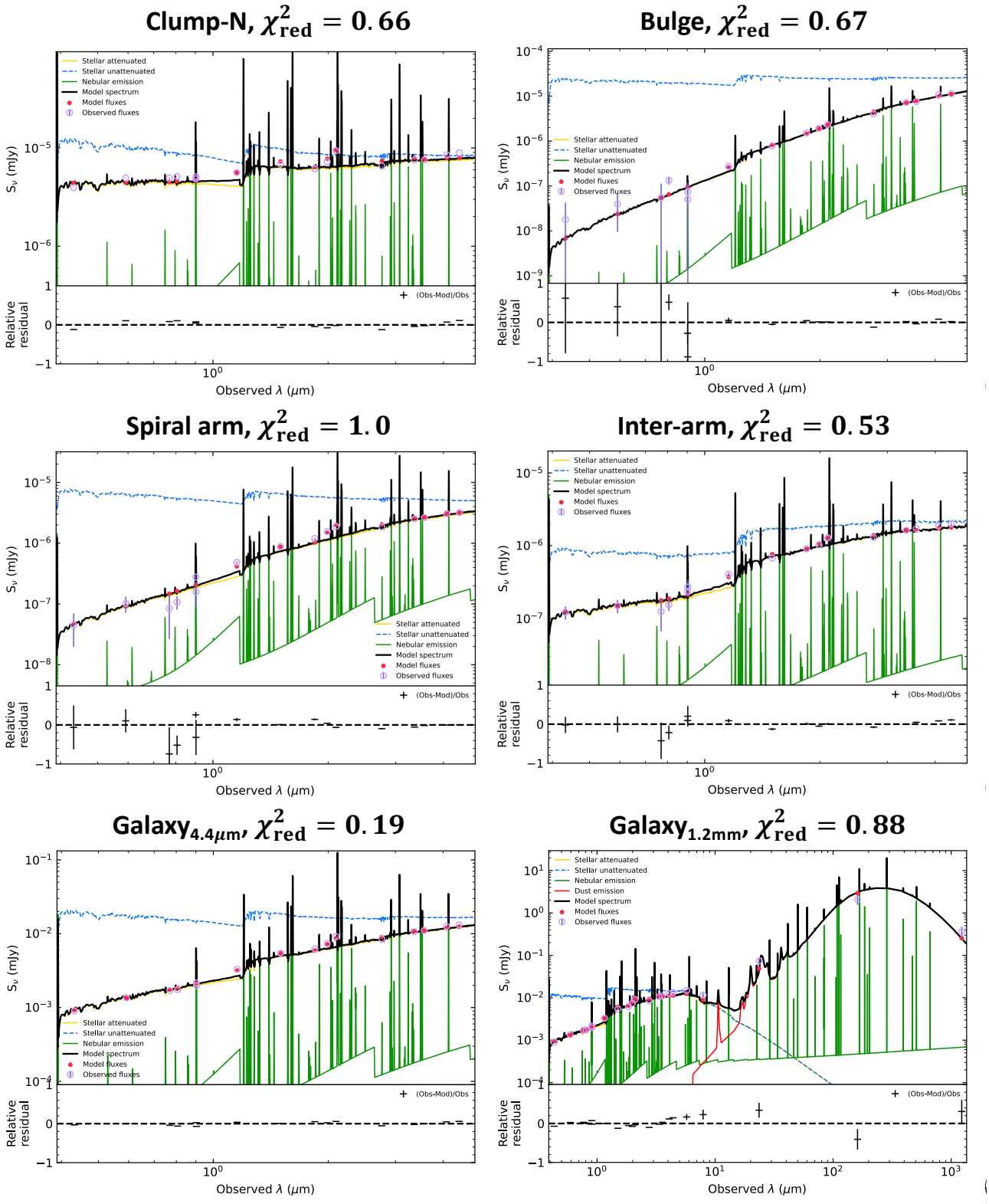

Fig. B.1. Best-fit models and observed SEDs as obtained from our resolved (top and middle panels) and integrated (bottom) SED modeling with CIGALE. *Top and middle.* Resolved results are shown for four representative pixels from four different regions, namely: Clump-N, the bulge, spiral arm, and inter-arm regions. The difference in the SED shape and in the relative intensities between distinct spectral components highlights the need for spatially resolved SED fitting to accurately account for the different physical properties of distinct galaxy regions. *Bottom*. Results from our integrated SED modeling of photometry up to 4.4 μm (left) and 1.2 mm (right), respectively.

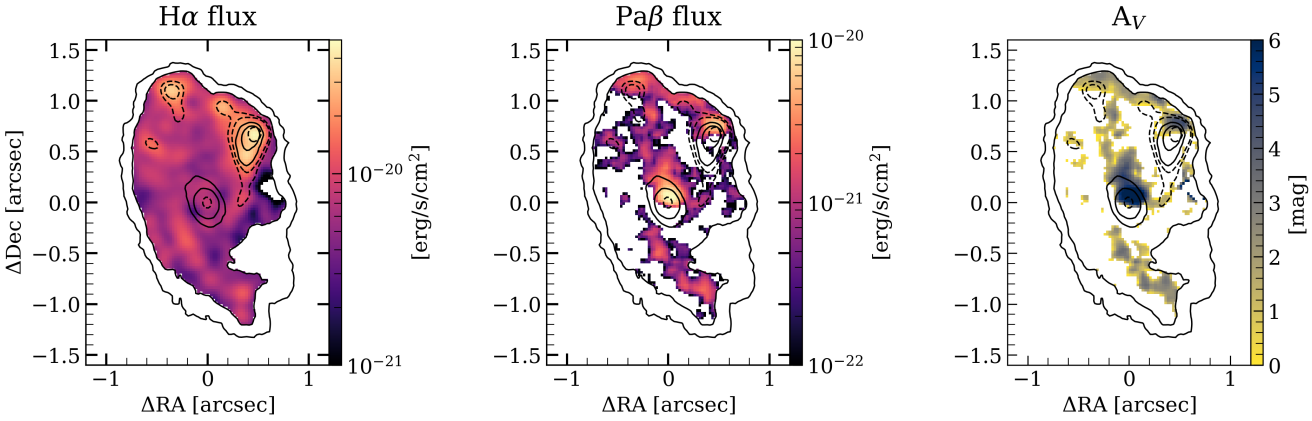

Fig. C.1. Line emission from medium-band F210M and F410M NIRCam imaging. From the left, we show maps of recovered Hα and Paβ line flux (not corrected for dust attenuation), and finally of nebular A_V, as inferred from Paβ/Hα line ratios. Black solid and dashed contours are the same as in Fig. 4.

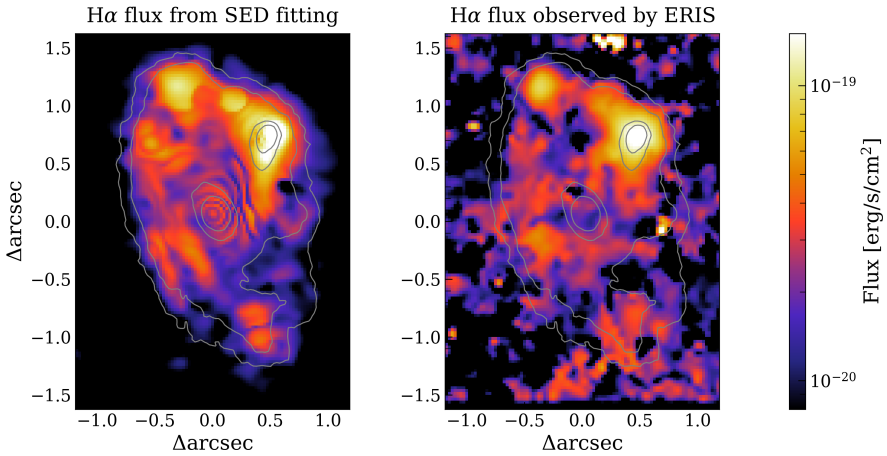

Fig. D.1. Expected observed Hα flux (left), as recovered from the SFR10 and $A_{V,\mathrm{star}}$ maps resulting from our spatially resolved SED fitting (see Fig. 4), and the real observed Hα flux from VLT/ERIS observations (right). Grey contours trace NIRCam F444W emission at 5%, 10%, 35%, 50% of the emission peak. Both maps have the same colorscale and a 0.025″ pixelscale.